Art of coloring glass with textures for photovoltaics

Aravind Swaminathan Balaji

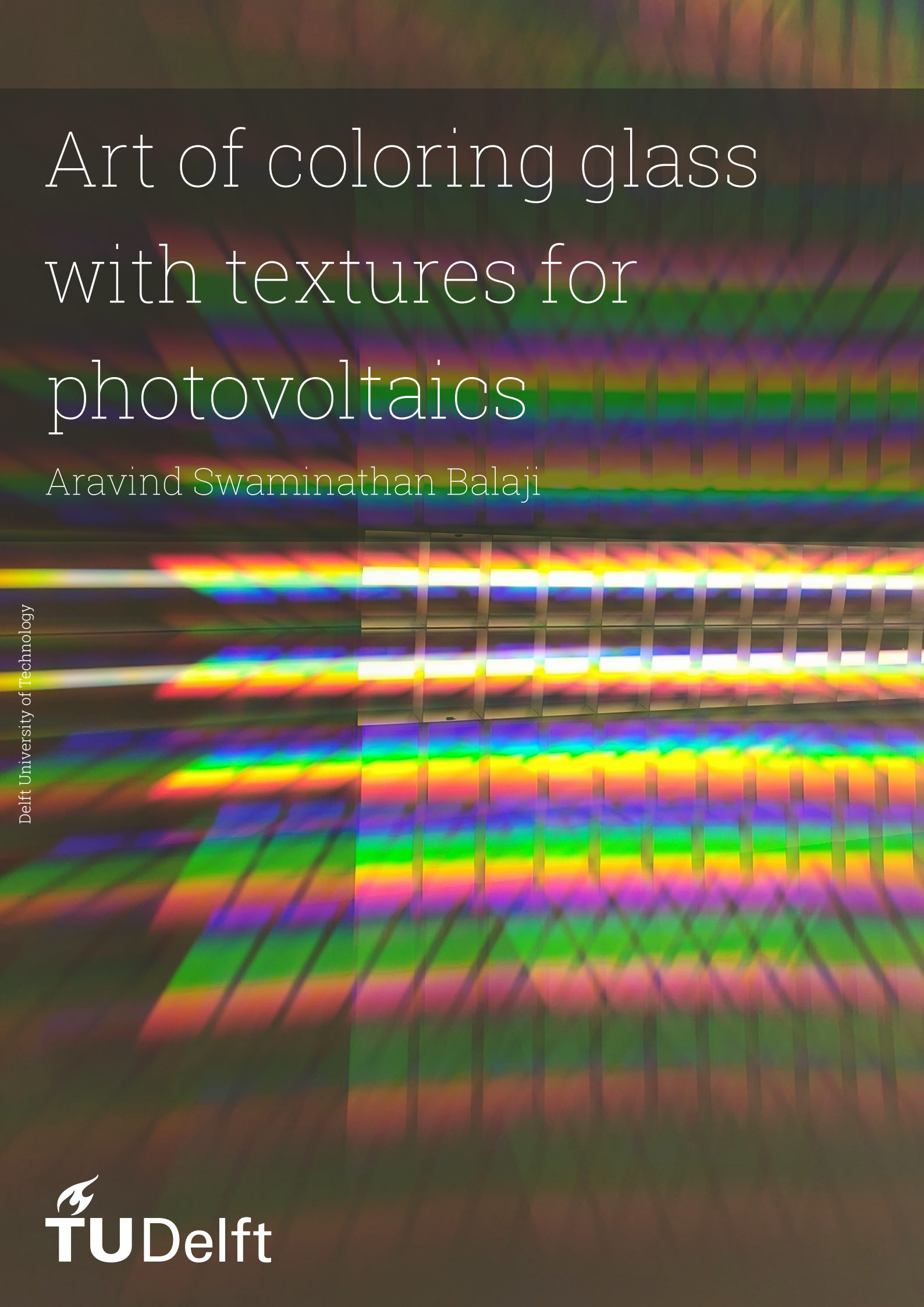

Delft University of Technology

TU Delft

Art of coloring glass with textures for photovoltaics

by

Aravind Swaminathan Balaji

to obtain the degree of Master of Science
at the Delft University of Technology,
to be defended publicly on Friday July 5, 2024 at 13:00.

Thesis committee:

Chair:	Prof. Dr. Ir. Arno Smets (PVMD)
Supervisors:	Prof. Dr. Ir. Arno Smets (PVMD)
	Ir. Govind PAdmakumar (PVMD)
External Examiner:	Dr. Arroyo Cardoso (EI)
	Dr. Moumita Rana (ESE)
	Dr. Paula Perez Rodriguez (PVMD)

Student number: 5705525

An electronic version of this thesis is available at `http://repository.tudelft.nl/`.

TU Delft

Acknowledgement

”The difference between something good and something great is attention to detail”

- Charles R. Swindoll

I carried out my graduation project with the PVMD group at the Delft University of Technology, as a part of my Master of Science in ”Sustainable Energy Technology”. Being involved in research has made me realise something that my mom has reiterated for a predominant part of my life, that to improve the whole of something, it is important to assess each and every minute detail and to try to optimise the same. This defines the entirety of this project in the most apt manner. I hope you enjoy reading this thesis and are able to acquire something of value.

I would like to convey my gratitude to my parents, to whom I will always be indebted to, for believing in me and supporting me in chasing my dreams and aspirations. I have to mention my fiance, Meenakshi Makhijani, who has been and will always be my ’North star’, ensuring that I stay on course, as I wade through the journey of my life. Amongst friends, there are one too many to be mentioned here, who have helped me and pushed me forward for the past two years. I am grateful to all of them, the ones present here and the others spread across the world, for being by my side and motivating me to complete this project.

I would like to thank my daily supervisor, Govind Padmakumar for honing my thinking and analytical skills and for his constant support, during the tenure of this project. In addition, I would like to extend my gratitude to Federica Saitta and Dr. Paula Perez Rodriguez for their unparalleled contributions and input. I also thank my supervisor, Prof. Arno Smets, for his valuable counsel and insights. I am grateful to Stefan G.M.Heirman, Tim Velzeboer, Engin Ozkol and Martijn Tijssen for being available always to deal with any issues that came up in the EKL and ESP lab. I would also like to convey my gratitude to Daniel van der Plaats and Johannes van Wingerden for helping me out on a technical and practical basis, whenever I faced any issues associated with the photolithography processing in the EKL. Finally, I also thank Dr.Arroyo Cardoso and Dr. Moumita Rana for attending my defense and evaluating my work and report.

Aravind Swaminathan Balaji

MSc - Sustainable Energy Technology

Delft, July 2024.

Abstract

The characteristic feature of ”thin” film solar cells is that they are thin, ranging over thicknesses of a few micrometers. This results in a drop in the light trapping capability of the solar cell, owing to the Beer-Lambert law. Thus, there is a need to optimize light management to enhance the amount of light being trapped in the photoactive region. This can be done by imparting texture in the glass superstrate to scatter the light and thereby allowing the light to travel over a longer distance in the absorber.

In this thesis, the focus is mainly on developing a high-quality reproducable procedure for achieving periodic texturing in glass and understanding the enhancement in the optical impact of the surface. the first objective was to understand the influence of the different processes involved in the fabrication procedure of periodic textured glass superstrates. This was done by varying the parameters associated with the individual processes and observing the resultant impact on the deterministic characteristics of the texturing process. The influence of the mask design, employed in the photolithography process, on the dimensionality of the texture was also analyzed. Based on the aforementioned results, an optimized recipe was developed and successfully implemented to enhance the depth of the periodic hexagonal texturing imparted onto the glass. Additionally, an indicative parameter Re/P was developed to imply the effect the processes had on the quality of the texturing.

This project also ventured into studying the growth of nanocrystalline silicon on the deep textures developed using the optimized recipe. Following this, an extensive optical analysis of the honeycomb textured superstrates was carried out to realize the scattering effect induced by this texturing on interacting with light. This was done by studying the transmittance components and the angular intensity distribution of the periodic textured glass. The interaction mechanism of the textures was found to be dependent on the wavelength and the size of the textures. In general, there was a linear increase in the diffuse transmittance with texture height, for all wavelengths of light. However, it was noticed that the slope of this relationship varied for the different wavelengths, since it was mainly dominated by different scattering mechanisms for different wavelengths. Finally, the influence of the optical impact of these hexagonal textures on solar cell performance was also studied by studying the Jsc of the micromorph tandem solar cells, developed on deep hexagonal textures of different periodicities.

Contents

List of Figures

List of Tables

Nomenclature

List of Abbreviations

a-Si	Amorphous Silicon
AFM	Atomic Force Microscopy
AID	Angular Intensity Distribution
ARC	Anti-Reflection Coating
ARTA	Automated Reflectance Transmittance Analyzer
BHF	Buffered Hydrofluoric Acid (BHF)
BIPV	Building Integrated Photovoltaics
BOE	Buffered Oxide Etch
c-Si	Crystalline Silicon
CdTE	Cadmium Telluride
CIGS	Copper Indium Gallium Selenide
CPV	Concentrator Photovoltaics
CZTS	Copper Zinc Tin Sulfide
DI	De-ionized
DSSC	Dye Sensitized Solar Cells
EKL	Else Kooi Lab
ESP	Electrical Sustainable Power Lab
F	Fluorine
GaAs	Gallium Arsenide
GW	GigaWatt
HF	Hydrofluoric acid
HMDS	HexaMethylDiSilazane
HNO_3	Nitric acid
IEA	International Energy Agency
InGaAs	Indium-Gallium-Arsenide
IPA	IsoPropanol
IS	Integrating Sphere
ITO	Indium Tin Oxide
i ZnO	intrinsic Zinc oxide

LPC	Liquid Phase Crystalline
LPCVD	Low Pressure Chemical Vapour Deposition
N2	Nitrogen
nc-Si	Nano-crystalline Silicon
NIL	Nano-imprint Lithography
NIR	Near Infra-red
PR	Photoresist
PV	Photovoltaics
RIE	Reactive Ion Etching
SD	Standard deviation
SEM	Scanning Electron Microscope
Si	Silicon
SiO_2	Silicon Oxide
TCO	Transparent Conductive Oxide
TDS	Technical Datasheet
TIR	Total Internal Reflection
UV	Ultra-Violet
WCA	Water Contact Angle

Symbols

ARp	Aspect ratio
H	Texture height
Hz	Haze
NI	Normalized Intensity
P	Periodicity of texture and hole in pattern
r	Hole radius in photoresist
Re	Equivalent hole radius
Td	Diffuse Transmittance
Ttot	Total Transmittance

1

Introduction

As per the IEA report on renewable energy sources that was published in 2023, the global electricity demand is expected to increase by an average of 3.4% annually till 2028, due to enhanced economic growth globally. This indicates a dire need for rapid acceleration in the decarbonization of the power generation sector. It is estimated that solar photovoltaics (PV) and wind will account for 96% of the installed capacity additions over this period, reaching almost 710 GW by 2028. This is depicted in the figure 1.1 below under the main case scenario in which the capacity additions are predicted while keeping in consideration the present challenges being faced across the globe in expanding the renewable power sector. [1]

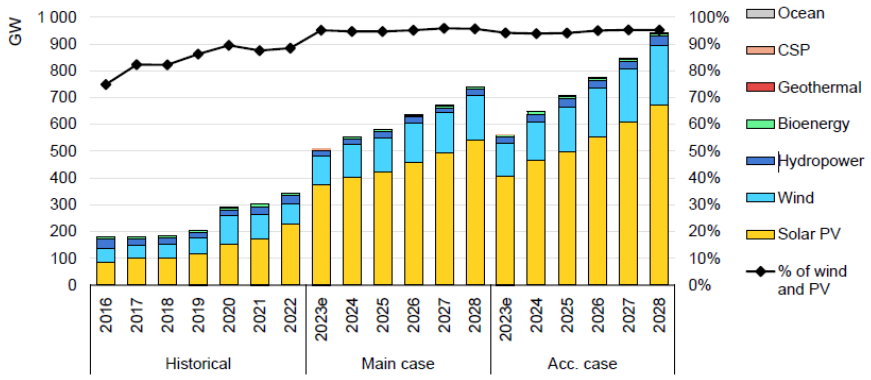

Figure 1.1: Estimated renewable capacity additions as per IEA Renewables 2023 report [1]

The PV market is mainly dominated by two main technologies, viz., crystalline silicon (primary) and thin film (secondary) solar cell technologies. As of 2023, the former constitutes around 90% of the PV market, while the latter constitutes the remaining 10%[2]. It is also to be noted that the crystalline Silicon technology has already reached conversion efficiencies of around 26.1%, which is close to the theoretical Shockley Quessier

limit of 29.4%. Thus, to increase the efficiency further, it is reasonable to go for tandem solar cells, which can achieve higher conversion efficiencies. It is more favorable to go for tandem solar cells in the thin film domain since these are already in existence. In addition, the flexibility of the thin film solar cells enables a broader field of usage, in comparison to the rigid crystalline silicon-based solar modules.[3]

As the name indicates, the thin film solar cell technology employs solar cells of thicknesses ranging from 3 - 4 μm, unlike the crystalline solar cell, which have solar cell thicknesses in the range of a few hundred micrometers. This is because the thin film solar cells majorly utilize amorphous and nanocrystalline silicon, which have diffusion lengths in the range of 100 to 300 nm. Thus, the thickness of such cells must be maintained within these limits to ensure efficient collection of the generated charge carriers. However, this implies that the amount of light collection, given by the Beer-Lambert law, will be much lesser, owing to the reduced thickness of the photoactive part in the solar cell. The absorption of the light can be increased by allowing the light to travel through the cell over a slanted path, in comparison to the perpendicular path it would generally take through the solar cell. This can be done by employing scattering of light at the front surface of the solar cell, which is ultimately achieved by texturing the substrate on which the solar cell is developed.

Two types of surface texturing can be imparted onto the substrate, viz., random and periodic texturing.[3] Since random texturing in photovoltaics has already been extensively studied, this project will primarily focus on honeycomb texturing in superstrates. The goal of this project is to optimize this periodic texturing in glass substrates, useful for thin-film solar cell production. The optimization will be done with the goal of efficient scattering of the entire spectrum of light, such that the overall conversion efficiency of the micromorph tandem solar cell can be further improved. The research questions addressed in this project are:

1. How do different physical steps in the photolithography process affect the texturing process of glass?
2. How does periodic texturing of glass superstrates affect the growth of nanocrystalline silicon?
3. Is it possible to create a dimensional relationship between the exposure mask dimensions and the dimensions of the periodic honeycomb texture obtained?
4. How does periodic texturing of glass superstrates affect the scattering of light? Is it possible to develop a relationship between the physical and optical parameters of the periodic texture?
5. How does a thin film silicon solar cell made on periodic textured superstrate behave optically?

The work done in the project is divided into 4 parts. Chapter 2 gives a brief overview of the theoretical principles and equipment details required to understand the work done in this thesis project. This chapter also gives a general description of the procedure used for imparting texture in substrates for thin film solar cells. This is followed by chapter 3 which focuses on the development of a fabrication process for obtaining hexagonal textured superstrates in glass. This chapter also discussed the optimization of the same to improve the physical characteristics of the textured superstrate. Then, chapter 4 dives into the characterization of the hexagonal textured superstrates developed in the previous chapter from an optical perspective. This chapter also offers the relationship found between the physical and optical parameters of the textured superstrate. Finally, chapter 5 offers the conclusions devised from the project and offers some recommendations for further enhancing the understanding achieved.

2

Theoretical background

2.1. Generations of solar cell technology

Solar cell technology can be broadly categorized into three different generations, based on the type of material used for the photoactive material [4] [3]. These are:

2.1.1. First generation solar cells

The first-generation solar cells primarily use crystalline Silicon as the absorber material. These can be further classified as mono-crystalline silicon (mono c-Si) and polycrystalline silicon (poly c-Si) solar cells. These are based on silicon material which has either a uniform lattice structure throughout the material (mono c-Si) or a random mix of lattice structures in the crystal. There is also another type that uses non-crystalline silicon material, which is referred to as amorphous silicon (a-Si). a-Si is a direct bandgap material with an energy bandgap of 1.7 eV, which is higher in comparison to c-Si of 1.1 eV. Thus it can absorb a greater part of the spectrum, increasing the spectral utilization.

2.1.2. Second generation solar cells

The second generation solar cells utilize thin film semiconductors as the absorber material and hence, are also called as thin film solar cells. As of 2023, the predominant thin film solar cell technologies are, namely, Cadmium Telluride (CdTe), Copper Indium Gallium Selenide (CIgS) and amorphous silicon. Along with these, Perovskites and Copper Zinc Tin Sulfide (CZTS) are also promising materials, being researched at present for their application in the thin film industry [4].

CdTe and CIGS have efficiencies higher than the c-Si solar cells due to their increased absorption coefficient in the visible spectrum as seen in figure 2.1, providing a more stable competition to the major player

in the photovoltaic field. However, the cost of these solar cells is a huge hindrance to the expansion of this technology, as the necessary resources like Indium, Cadmium, etc. are rare elements and are expensive [4]. It is to be noted that as of now, the highest conversion efficiency achieved so far, around 47.6% is by a quadruple junction solar cell, based on the GaAs technology, coupled with concentrator photovoltaics (CPV) [5].

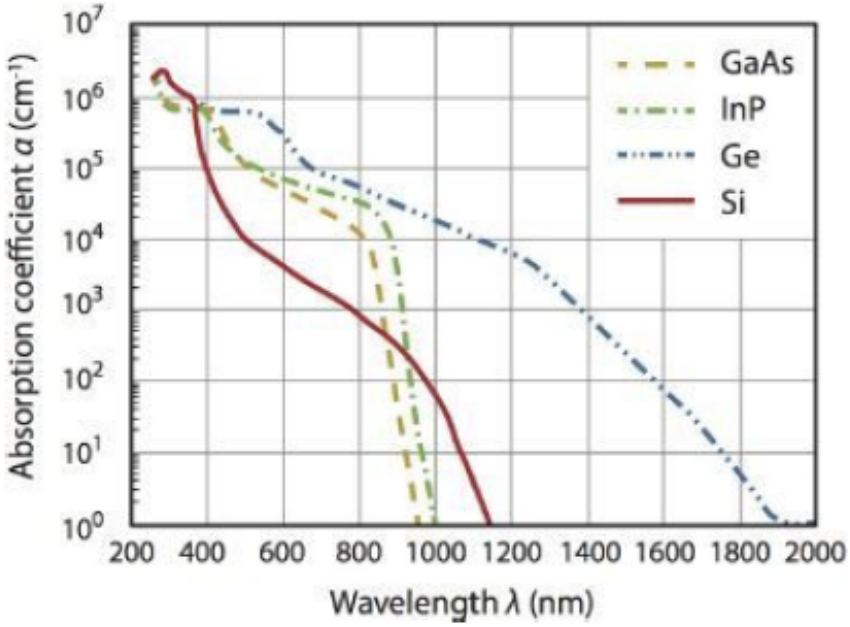

Figure 2.1: Absorption coefficient of different semiconductors[3]

2.1.3. Third generation solar cells

The third generation of solar cells is a relatively new field of solar cells that are in development. These include dye-sensitized solar cells (DSSC), quantum dot structures and perovskite-based polymer solar cells. These perovskite-based solar cells, when used in tandem with the c-Si solar cells have been recorded to provide a conversion efficiency of around 33.9 %, which exceeds the Shockley-Queisser limit of single junction c-Si solar cell. [6]

However, the major disadvantage associated with the perovskites is their degradation on exposure to UV radiation and moisture, which can lower their efficiency considerably.

There is a constant need to promote the acceptability of solar technology and this can be done by improving conversion efficiency. The methods to achieve this are discussed in the upcoming section 2.2.

2.2. Ways to promote efficiency

The three main design rules to be considered when developing a solar cell are a) Badngap utilization, b) Spectral utilization and c) Light management.[3]

The bandgap utilization indicates the actual portion of the available bandgap, which is a characteristic of the

photoactive material, that is used in the solar cell. This is affected by the dominant recombination mechanism present in the material, which is in turn influenced by the concentration of defects and the type of bandgap the chosen material has. The wavelengths of light that are absorbed are determined by the bandgap energy of the photoactive material, as only light particles with an energy equal to or above this can be absorbed by the material. It is also to be noted that this can be further enhanced by using multi-junction solar cells, thereby reducing the excess energy loss in the solar cell.

Light utilization can be improved by ensuring that the design of the solar cell is in such a way that the optical losses are minimized. This can be done by using ARC (Anti-Reflective Coating), which uses the concept of refractive index grading and constructive-destructive interference to decrease the amount of light reflected from the front side of the solar cell [3]. Another method that can optimize light management is to introduce surface texturing at the interface, thereby enhancing the in-coupling of the light in the solar cell.

In this project, this particular application of surface texturing to enhance the conversion efficiency of thin film solar cells is considered and studied further.

2.3. Surface Texturing in glass

The mechanism by which texturing influences the light in-coupling can be understood from the interaction of light at an interface between two media.

2.3.1. Optical interaction at an interface

The macroscopic interaction of light is represented in the following image 2.2.

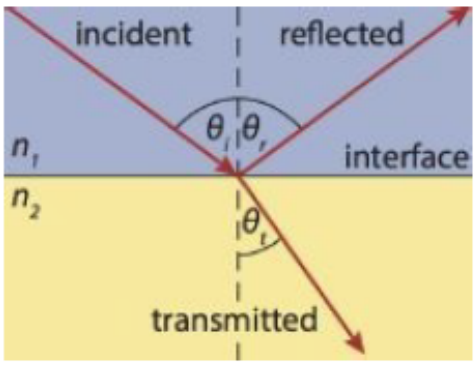

Figure 2.2: Interaction of light at an interface

The wave-particle duality of light implies that light can be considered as an electromagnetic wave and also as a packet of particles, possessing particular values of energy. For the interaction of ligth with an interface, let us consider the wave nature of light. According to the Maxwell equation[3], light can be represented as:

$$\left(\frac{\delta^2}{\delta x^2}+\frac{\delta^2}{\delta y^2}+\frac{\delta^2}{\delta z^2}\right)\zeta-\frac{n^2}{c_0^2}\left(\frac{\delta^2\zeta}{\delta t^2}\right)=0 \tag{2.1}$$

$$\left(\frac{\delta^2}{\delta x^2}+\frac{\delta^2}{\delta y^2}+\frac{\delta^2}{\delta z^2}\right)\epsilon-\frac{n^2}{c_0^2}\left(\frac{\delta^2\epsilon}{\delta t^2}\right)=0 \tag{2.2}$$

Here, ζ describes the magnetic field, ϵ describes the electric field, c_0 the speed of light in vacuum, n describes the refractive index and t describes the time with light propagating along the z direction.

When such an electromagnetic wave contacts a flat interface between two media, some part of the light will be reflected, while the remaining portion will be refracted into the next medium. In the case of reflection, the light component would just bounce back along a path, such that the angle of reflection is equal to the angle of incidence.

In the case of refraction, the interaction is described by the Snell's law[3], given in equation 2.3. Here, it is to be noted that the refractive indices are considered to be constituted only by the real component while the imaginary component is neglected. This is because at an interface, it can be assumed that no absorption occurs and hence the imaginary part, consisting of the extinction coefficent κ is not considered. The Snell's law is given by:

$$n_1 \sin\theta_1 = n_2 \sin\theta_2 \tag{2.3}$$

In the above equation, n_1 and n_2 indicate the refractive indices of the two media and θ_1 and θ_2 refer to the incident and refraction angles of the light with the normal to the interface in the respective medium. The intensities of the light components that are reflected (r) and refracted (t) are provided by Fresnel equations, given in equations 2.4 and 2.5, which are also dependent on the type of polarisation the light is composed of. Here, p indicates the component of light that is polarised along the path of propogation and s indicates the polarised component of light that is normal to the path of propogation.

$$r_s=\frac{n_1\cos(\theta_i)-n_2\cos(\theta_t)}{n_1\cos(\theta_i)+n_2\cos(\theta_t)}, r_p=\frac{n_1\cos(\theta_t)-n_2\cos(\theta_i)}{n_1\cos(\theta_t)+n_2\cos(\theta_i)} \tag{2.4}$$

$$t_s=\frac{2n_1\cos(\theta_i)}{n_1\cos(\theta_i)+n_2\cos(\theta_t)}, t_p=\frac{2n_1\cos(\theta_i)}{n_1\cos(\theta_t)+n_2\cos(\theta_i)} \tag{2.5}$$

Following this, the total intensity of light that is reflected (R) and transmitted (T) are calculated using equations 2.6 and 2.7 respectively.

$$R=\frac{1}{2}\left(r_s^2+r_p^2\right) \tag{2.6}$$

$$T=1-R=\frac{n_2\cos(\theta_t)}{2n_1\cos(\theta_i)}\left(t_s^2+t_p^2\right) \tag{2.7}$$

It is also to be noted that when light travels from an optically lighter medium to a denser medium (n1 < n2), there is a particular angle of incidence beyond which all light will be reflected into the first medium. This is called the critical angle for the media and the resulting phenomenon is referred to as total internal reflection (TIR)[3]. The equation for the critical angle is represented numerically in the following equation 2.8.

$$\theta_i=\sin^{-1}\left(\frac{n_2}{n_1}\right) \tag{2.8}$$

2.3.2. Microscopic optical interaction

As mentioned earlier, the above equations represent the macroscopic interaction of light with an interface, implying the condition where the scale of the surface features is much larger than the wavelength of the incident light. However, when we consider the cases where the particle size is on a scale comparable with the wavelength of the incident light, then the interaction is not governed by the Fresnel equations anymore. In this case, the Mie and the Rayleigh scattering come into effect.

The intensity of light scattered at an angle θ by a particle is given by the equation 2.9 below.

$$I(\theta) = I_o \left(\frac{2\pi}{\lambda}\right)^4 \left(\frac{n_p^2 - n_0^2}{n_p^2 + 2n_0^2}\right)^2 \left(\frac{d}{2}\right)^6 \frac{1 + \cos^2\theta}{2R^2} \tag{2.9}$$

Here, λ indicates the wavelength of the incident light, n_p indicates the refractive index of the particle, n_o indicates the refractive index of the surrounding medium, d indicates the diameter of the particle and R indicates the distance to the particle from the light source.

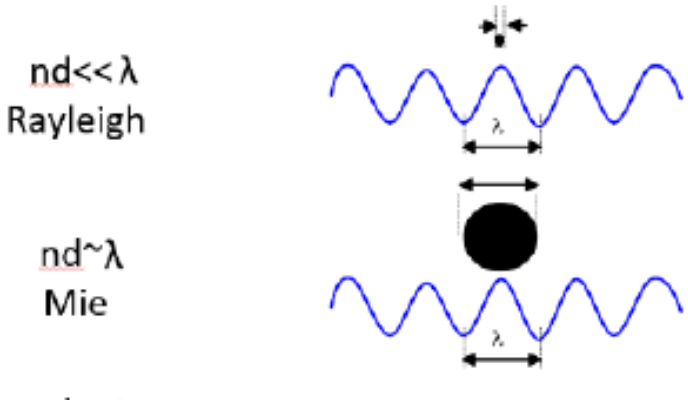

Figure 2.3: Rayleigh vs Mie scattering [3]

The figure 2.3 indicates that the relationship between the particle size and the wavelength of the incident light determines the type of scattering that occurs.

When the size of the particle is much smaller than the wavelength of light, then Rayleigh scattering occurs. In such a case, from equation 2.9 it can also be seen that the scattering is heavily dependent on the wavelength, implying that quantifiable amounts of scattering will occur across all the scattering angles, as can be seen in the bottom image in figure 2.4.

On the other hand, when the size of the particle is comparable to the wavelength of the incident light, Mie scattering occurs. In this case, the scattering is affected by the size of the particle. The equation 2.9 also shows that the influence of the scattering angle on the scattering intensity increases, where the scattering towards the front increases, with an increase in the size of the particle. This can also be visually seen in the figure 2.4, as we move from the bottom (c) to the top (a) [7].

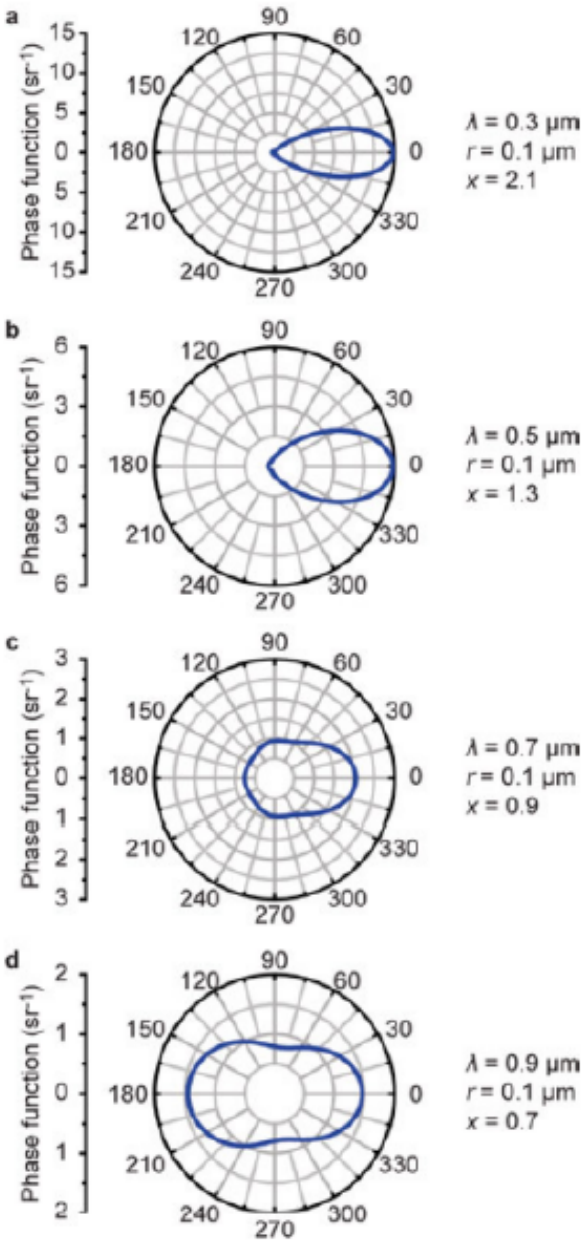

Figure 2.4: Difference in scattering pattern: Mie to Rayleigh transition (a to d) [7]

2.4. Optical interaction in texture interface

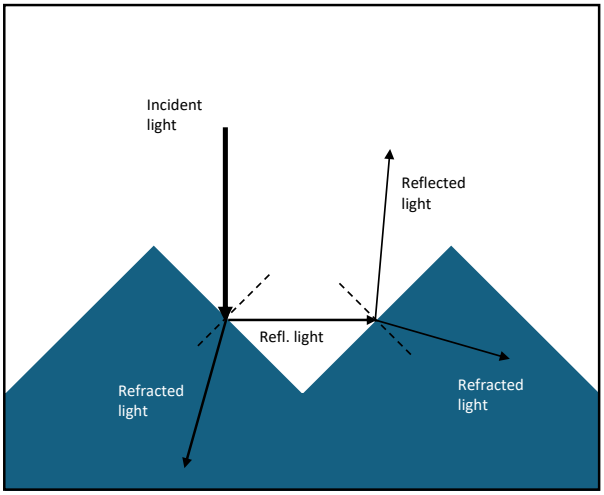

Figure 2.5: Interaction of light with texture interface

The textured surface is considered to have macroscopic interaction with light. Hence, the Fresnel and Snell laws are considered to understand the impact of the texture on the scattering of light. The main advantage of the textured surface over the flat surface is that, light that is perpendicularly incident on a texture could be reflected to another part of the textured surface, thereby reducing the reflection losses. An example of this is shown in figure 2.5, where a higher amount of light is entering the second medium, in comparison to a flat surface interface.

The textured glass can be classified according to the size of the texture and the uniformity of the texture across the surface. Based on the uniformity, the texture can be random or periodic indicating the repeatability of the same across the surface. The methods used for obtaining these different types of textures are explained below.

2.4.1. Random texturing in glass

The texturing process is referred to as random texturing when the surface is textured in a manner where there is less control over the positioning and uniformity of the texture on the surface. The most commonly used method for obtaining random textures in substrates is sacrificial texturing. [8] In this method, a sacrificial layer, which is usually crystalline is deposited onto the substrate. The deposition can be done by using physical processes like sputtering, LPCVD (Low-Pressure Chemical Vapour Deposition), etc. The substrate and the sacrificial layer are then exposed to an etchant solution, which is composed of two chemicals, one that can etch the sacrificial layer and the other that can etch the substrate. Due to the crystalline nature of the sacrificial layer, the second etchant will flow through the crystal boundaries and come in contact with the substrate

surface at different instances of time. This will continue till the sacrificial layer is completely etched away by the first etchant chemical. As a result, the texture size and the depth of the texture obtained will be spatially random across the entire substrate surface.
It is to be noted that the properties of the texture obtained will be dependent on the crystal size, lattice orientation and other properties of the sacrificial layer. These can be used to control the type of texturing required on the substrate. Some examples of such texturing include:

- ITO texturing - used to produce micro textures in glass superstrates
- iZnO texturing - used to produce nano textures in glass superstrates

2.4.2. Periodic texturing in glass

As the name implies, this type of texturing is periodic and reproduced across the substrate's entire surface of the superstrate. Photolithography and wet etching are the main steps involved in achieving this type of texturing. A detailed description of the steps involved in periodic texturing is provided in section 3.1.

2.4.3. Periodic vs random texturing

The main disadvantage of random texturing is that it is difficult to predict the extent of texturing that can be obtained since the texturing process is highly influenced by the crystallinity of the sacrificial layer that is used. This has a direct influence on the defect density in the silicon and can impact the efficiency of the solar cell. This makes it more complex to model the solar cell performance based on random texturing.
In contrast, periodic texturing offers an ample amount of control and predictability about the uniformity and the dimensional aspects of the texture. The design parameters of the mask can be correlated to the expected texture dimension and thus, the required superstrate configuration can be obtained by using the appropriate reticle design.
Another important point that pushes periodic texturing as a better alternative is the presence of a flat surface in the center of these textures. These regions reduce the presence of cracks in the nc Si growth, as the perpendicular growth of this layer from the superstrate occurs with minimal intersection of the growth vectors, corresponding to individual points on the superstrate[9]. This reduction in the cracks and defects in the photoactive material helps to reduce the bulk recombination losses associated with the solar cell. This helps to enhance the Voc of the solar cell and improves the overall conversion efficiency, as well.

2.5. Photolithography: an Overview

Photolithography is a fabrication process that is employed in the manufacturing of patterned thin film substrates, which are then utilized in various fields like biosensors, microelectronics, thin film solar cells, etc. This

process generally involves coating a thin photoresist (PR) layer on the substrate surface, and then exposing the same to UV radiation through a patterned reticle, that has the same pattern as the required design to be imprinted onto the substrate. Following this, depending upon the type of photoresist, the exposed or the non-exposed parts will become soluble in an organic developer, which is then used to remove the same, thereby obtaining the required PR pattern on the substrate. The basic steps that are generally involved in the process of photolithography are:

1. Preparation of the substrate surface

   Before moving on to the photolithography process, it is essential to prepare the surface of the substrate accordingly. This can be done by using some or all of the following steps[10]:

   - Cleaning of the surface with an appropriate reagent to remove any impurities.
   - Dehydrating the surface to remove water molecules that are present on the surface. This is essential to improve the adhesion of the non-polar photoresist to the surface of the substrate. The presence of water inhibits this. This is because water is a polar molecule and will attach itself to the oxidized surface of the substrate, thereby preventing the photoresist from being bonded to the surface of the substrate. The dehydration can be done by heating the substrate at elevated temperatures for specified durations, depending on the substrate used.
   - Another preparation step involves priming the surface by exposing the surface to a primer, which also helps to improve the PR adhesion to the substrate surface. This step is not always essential but is recommended to ensure effective adhesion of the photoresist to the substrate. The primer is generally applied as a vapor and a commonly used example of the same is HMDS (HexaMethyldiSilazane).

     The working of the HMDS is shown in figure 2.6 below. The HMDS hydrolyses in the presence of adsorbed moisture to form trimethyl silanol and ammonia [11]. This is because the trimethylsilyl groups bond with the oxygen on the surface while the hydrogen is taken away by the NH group, forming ammonia as a byproduct. While the Si atom is attached, the methyl groups are left facing outward, creating a non-polar hydrophobic surface. In this way, the HMDS removes the hydroxyl groups present on the surface and also makes the surface more adhesive for the photoresist [12] [13].

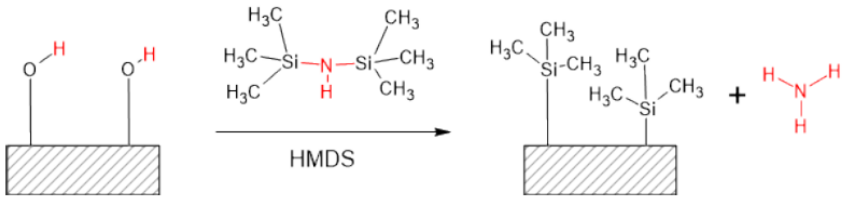

Figure 2.6: Working principle of HMDS [11]

2. Coating of Photoresist on substrate

   The first step in the photolithography process is to coat the layer of PR onto the substrate surface, such that, it is of the required thickness and it is uniformly coated onto the substrate.

   The coating process can be done by either using spin coating or spray coating. However, the spin coating method is more commonly used, as it uses centrifugal force to ensure that a uniform thickness can be obtained for the photoresist layer being coated on the surface[14]. This also provides better control on the thickness of the photoresist as the thickness of the photoresist is mainly determined by the spin speed of the substrate and the dispense volume of the photoresist, which can be varied accordingly.

3. Exposure of coated substrate to UV

   The next step in the photolithography process is the exposure of the coated substrate to Ultraviolet light through a patterned reticle. The photoresist is a light-sensitive material and the reaction of the same on exposure to UV depends on the type of PR being used. In the case of a positive PR, the exposure to UV light changes the chemical structure of the same, causing it to become more soluble in the photoresist developer. Alternatively, for a negative PR, the UV exposure causes the exposed parts of the PR to polymerize and harden, thereby making them more difficult to dissolve in the developer solution. Thus, in the case of a positive PR, the pattern in the reticle is transferred onto the substrate post-development. However, when a negative PR is used, a reverse image of the reticle can be obtained on the substrate post-development.

   It is preferred to use positive photoresists in applications that require high-resolution patterning. This is because positive PR can withhold the pattern since the developer solution permeates only through the exposed regions of the PR. On the other hand, for negative PRs, pattern distortions can occur due to both exposed and non-exposed parts of the PR being permeated during the development step [15].

4. Development of the exposed parts

   The development is the final step in the photolithography process. In this step, the exposed PR is acted upon to form the patterned PR onto the substrate. This can be done by dip developing or spin developing. The spin-developing process is preferred as it ensures a uniform development rate across the entire surface and also helps to ensure the complete removal of the developed parts of the PR [16].

2.6. Atomic Force Microscopy

Atomic Force Microscopy (AFM) is a high-resolution non-optical imaging method, which helps us to get an accurate depiction of the surface morphology, up to a nanometer scale. It allows accurate and non-destructive measurements of the surface properties in air, liquids or ultrahigh vacuum. The operating principle of the AFM is visually represented in figure 2.7 below.

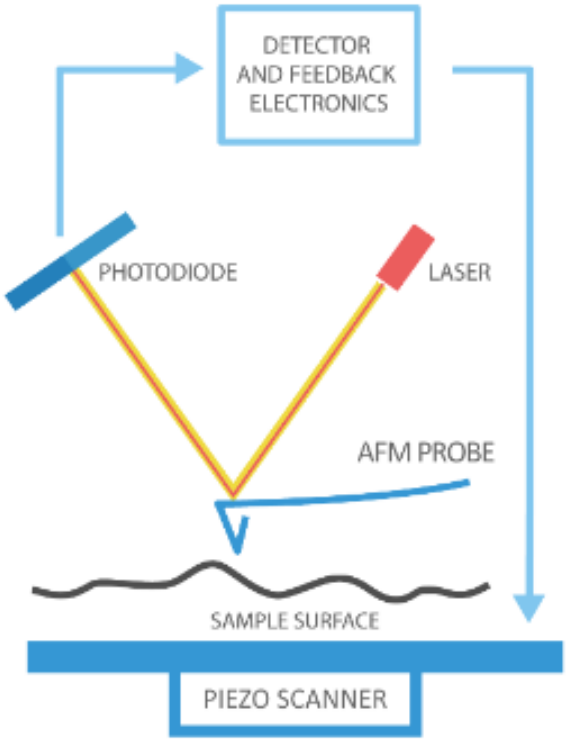

Figure 2.7: Operating principle of AFM [17]

The AFM measurement process involves scanning an AFM probe with a sharp AFM tip in a raster manner on the sample surface. The AFM probe tip is to be selected based on the mode of measurement and the surface morphology to be measured. This tip is fixed onto the probe in a free cantilever manner. The lateral and vertical position of the AFM probe is controlled by a piezoelectric scanner. There is also a laser which is reflected from the backside of the tip and this reflected component is directed to a photodiode. There are three main modes of operation, viz. contact mode, semi-contact mode and tapping mode[18]. For our measurement, the contact mode is used since the glass surface is hard enough to not be impacted by the tip and also since this mode offers the most accurate depiction of the surface profile. As the probe tip comes in contact and moves along the surface, the vertical deflection of the same is sensed by the variation of the reflection component in the photodiode. A feedback loop controls the vertical position of the probe to ensure constant deflection of the AFM tip, resulting in a constant interaction force. The coordinates that are tracked by the AFM along the scan surface are combined with the height data to generate a topographic image of the surface.

2.6.1. Honeycomb imaging methodology

The AFM probe tip used for imaging the surface morphology of the honeycomb textures is Fastscan-A. This particular probe tip is used as it offers high resolution and short imaging time. It was also attempted to capture

AFM images using scanasyst-air tips, but the system could not process the samples properly. The positioning of the sample on the sample stage is to be done such that the textured surface faces the tip side and the primary flat is facing to the right, towards the control mechanism of the stage. This is done so that the path taken by the probe tip during the raster is along the axis in which the deepest profile can be measured. The orientation is pictorially represented in figure 2.8.

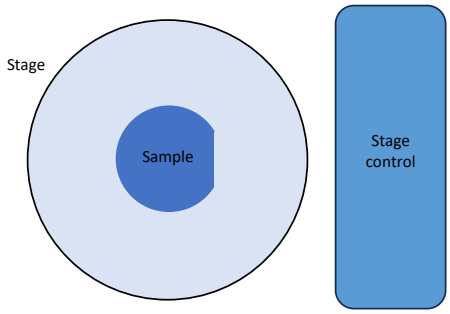

Figure 2.8: Representation of sample orientation for AFM measurement

The maximum measuring limit of the equipment is 30μm, and a scan size of 16μm was chosen since this would ensure multiple honeycombs being imaged, while also being well within the scan limit of the equipment. Post measurement, the AFM image thus obtained could be analyzed using the Nanoscope software. Here, the first step was always to level the measurement data, so that the reference for the height data is along the same line across the scan area. This can be done by using the ”Plane Fit” option provided in the toolbar. Post this, the section tool can be used to obtain the section along any specific axis to visualize the profile along that axis.

2.7. Scanning Electron Microscope (SEM)

High-resolution images of the textured surface have been obtained using the Hitachi Regulus 8230 SEM present in the EKL. A schematic representation of an SEM is provided in figure 2.9 [19]. The SEM uses a collimated beam of high kinetic energy electrons to study the surface aspects on a micrometer or nanometer scale. These electrons interact with the specimen surface to produce different kinds of emissions like secondary electrons, backscattered electrons, etc. These electrons are then captured by appropriate detectors and used to obtain an image of the sample surface.

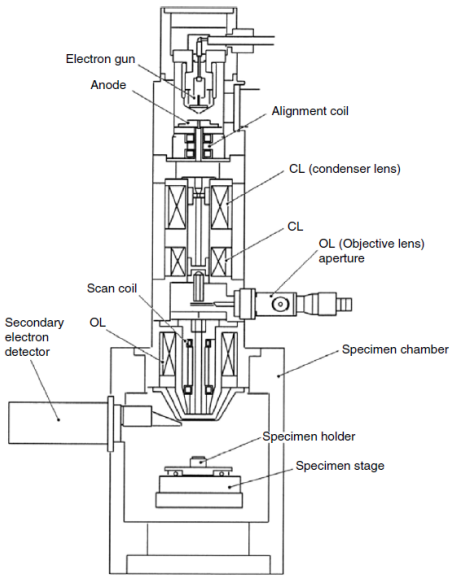

Figure 2.9: Schematic representation of a SEM [19]

2.8. Physical parametrization of periodic textures

Aspect ratio (ARp)

The aspect ratio can be defined as the ratio of the maximum texture height to the lateral width of the texture. In the case of periodic textures, the width of the texture is equal to the periodicity of the holes in the mask and hence can be replaced by the same. Thus, the texture aspect ratio can be depicted as

$$ARp = H/P \tag{2.10}$$

Texture height (H)

The texture height is taken as the highest value of the depth in the texture. It is measured from the AFM scan of the superstrate surface, by taking a section profile along the green and red axis, as mentioned earlier.

Slope distribution

The probability distribution of the surface slopes across the area of the AFM scan is also measured using Gwyddion software. The accuracy of this slope distribution was vetted by a code developed on MATLAB, to achieve the same purpose. This has been added in the appendix A. This gives us an understanding of the sharpness of the surface in the textured superstrate, which could affect the silicon growth.

2.9. Optical parametrization of periodic textures

Total transmittance (Ttot)

Total transmittance refers to the total intensity of the transmitted light that is transmitted by the substrate when light is incident on it. It is measured by using the Perkin Elmer Lambda 1050+ UV/Vis/NIR spectrophotometer with the Integrating sphere, present in the ESP lab. This equipment is provided with a tungsten-halogen and deuterium lamp and can work in the spectrum range of 175 nm to 3300 nm [20]. The equipment is also provided with an Integrating Sphere (IS), coated with Spectralon. For measuring the Ttot, the sample is kept in between the source and the IS, with the textured surface facing the IS. The back side of the IS is closed with a spectralon disc to ensure that all the light transmitted by the sample is trapped and sensed by the detector. The equipment has two detectors for sensing light from different regions of the spectrum. An InGaAs-based detector senses light above a wavelength of 850 nm while a PhotoMultiplier Tube detector is used for sensing light below a wavelength of 850 nm.

A schematic representation of the Perkin Elmer Lambda 1050+ spectrophotometer is shown below in figure 2.10.

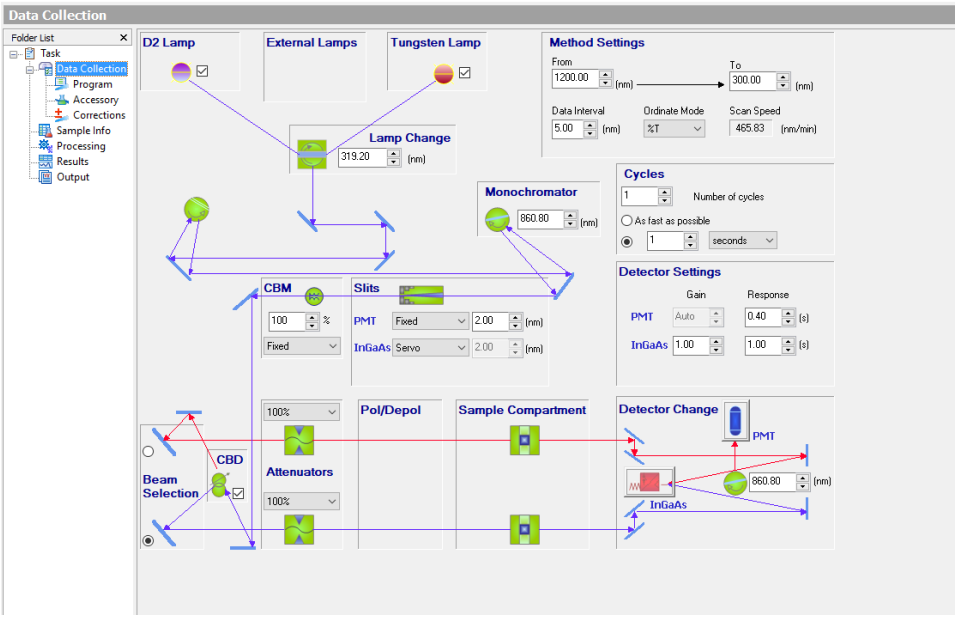

Figure 2.10: Schematic representation of Lambda 1050

Diffuse Transmittance (Td)

Diffuse transmittance refers to the intensity of the transmitted light that is scattered away from the initial linear path after the light passes through the substrate. It is also measured by using the Lambda 1050+ spectrophotometer, similar to the total transmittance (Ttot). However, the difference in the measurement process is that the spectralon back reflector in the IS is removed, thereby allowing the specular component of the transmitted light to remain undetected by the detector. This ensures that only the diffuse component of the

transmitted light from the sample is detected.

Haze (Hz)

Haze (Hz) is the ratio of the diffuse transmittance (Td) to the total transmittance (Ttot) measured at each wavelength. It is an indication of the percentage of the total transmitted light, that is scattered by the sample. This helps to understand how much scattering is caused by the texture as the light passes through.

Angular Intensity Distribution (AID)

The AID helps us to visualize the scattering effect caused by the sample on s and p-polarized light of different wavelengths. It provides the percentage of intensity of light that is detected after interacting with the sample at a range of detector angles. It is measured using the Automated Reflectance Transmittance Analyzer (ARTA) present in the ESP lab. The schematic representation of the same is shown in figure 2.12. Here, it is clear that the main difference in the setup, when compared to that of the Lambda is the presence of a polariser, which helps to polarise the monochromatic beam into s (perpendicular) and p (parallel) polarized light. The polarization is essential since the scattering effect caused by the texture will be different, depending upon the polarisation of the light incident on the same.

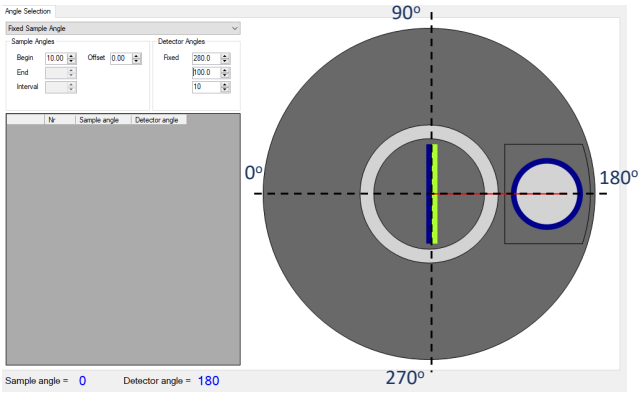

Figure 2.11: Schematic representation of Variable angle detector setup

The ARTA offers the scope of measuring the AID in the Transmittance (T) or Reflectance (R) mode. This is enabled due to the presence of a Variable angle detector setup in the ARTA. The angular span within which the detector moves during the measurement determines the type of measurement being done. This is represented in figure 2.11

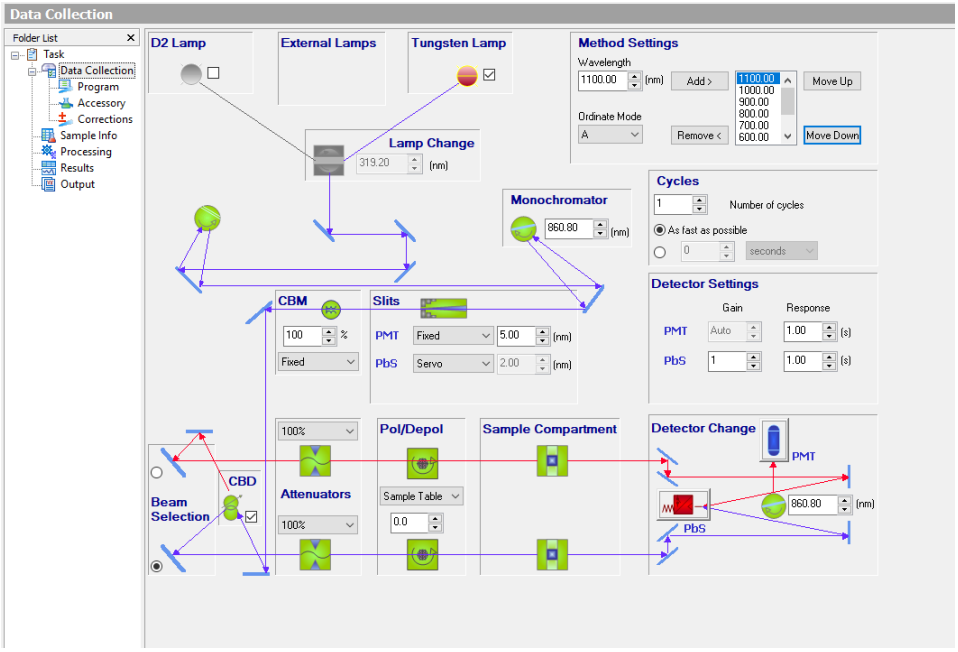

Figure 2.12: Schematic representation of ARTA

For our characterization, the AID is measured in Transmittance mode, implying that the detector will be moved in the second and third quadrant (90^o to 270^o), in steps of 10^o. The flat surface of the superstrate is kept facing the source so that the scattering by the interaction of the light with the textured surface on the back side of the superstrate can be characterized. This is done, as in a solar cell, this surface would be present at the interface between the superstrate and the Transparent conducitve oxide (TCO). The detector and source slit width settings are set as per previous work done.[21]

3

Design of honeycomb texturing

Hexagonal texturing is a surface texture morphology that has been incorporated into different materials using various processing methods to achieve different applications. Y. Wang et al. were able to obtain hexagonal texturing in Titanium using the process of laser ablation. In this process, a nano-pulsed fiber laser beam would travel in a hexagonal pattern on the surface and the resulting thermal energy would result in the melting and evaporation of the material along the path of the laser. This was mainly done to reduce the reflectance of the surface, by more than 90% in the wavelength range of 650 - 1100 nm [22].

E. Manea et al. studied the effect of hexagonal texturing on the front side of silicon-based solar cells to reduce the front reflectance of these solar cells. The hexagonal texturing was obtained by growing a 1000nm Silicon oxide layer and patterning the same using photolithography to obtain a patterned Silicon oxide mask layer with 4μm dia holes, spaced out by 20 μm along the horizontal and 60^o direction. Following this, the patterned Silicon substrate was wet etched isotropically using (HNO_3:HF:CH_3COOH—25:1:10) acid solution to obtain hexagonal features with an ARp of 0.35 [23].

H.Sai et al., T. deVrijer et al. and Eisenhauer et al. have extensively researched the application of honeycomb-based periodic textures in thin film solar cells [24] [25] [26] . H. Sai used a similar approach as E. Mania et al. to obtain hexagonal texturing in Silicon, which were then used as superstrates for growing n-i-p μc-Si:H solar cells. The difference in the texturing process is that the wet etching of the silicon surface was done anisotropically by using BHF. They concluded that the substrates with an Aspect ratio (referred to as ARp) in the range of 0.2 to 0.25 and with a periodicity (referred to as P) higher than the thickness of the solar cell by 0.5 μm gave the best optical and solar cell characteristics. This ARp range was noted to be optically optimum as well since the reflectivity started dropping for values outside of this range. The conclusion that the P must be higher than the cell thickness was required to ensure that the cells do not become flat on the

top and still follow the hexagonal pattern [24]. D. Eisenhauer et al. developed an alternative method for the hexagonal texturing of Liquid Phase Crystalline (LPC) silicon thin-film solar cells on glass based on a combination of nano-imprint lithography (NIL) and reactive ion etching (RIE). A nano-imprinted resist layer was used as a three-dimensional etching mask to obtain a similar pattern in the c-Si absorber surface by reactive ion etching. Using this method, the honeycomb textures were obtained with periods between 1.5 µm and 6.0 µm and ARp ranging from 0.1 to 0.3. It was concluded that the textured surface with a period of 6.0 µm and a height-to-period ratio of 0.2 was the most optimum for solar cell performance, providing a short-circuit current density of 28.7 mA cm−2 [26]. Similarly, T. de vrijer et al. developed a methodology for producing honeycomb textures in silicon and devised a relationship between the design of the mask and the texture dimension that can be obtained. They are also supported by the conclusions of H.Sai et al., that the ARp of 0.2 - 0.25 range is the optimum for optical in coupling in solar cells. It was also concluded that there is a specific maximum thickness of the nc-Si for a particular honeycomb design, until which the growth can be maintained crack-free. This is mainly dependent on the periodicity of the hexagonal texture in the substrate being used and again concurs with the conclusions of H. Sai et al. [25] [24].

In this chapter, we discuss the methodology developed for fabricating the honeycomb textured superstrates. The first section describes the method developed for producing the honeycomb textures in glass superstrates. The second section 3.3 indicates the different experiments that were carried out for adhesion promotion in the photolithography process and the resulting improvements.

3.1. Basic methodology for honeycomb texturing

The methodology for producing honeycomb textures in the glass superstrates was derived from the work of H.Sai et al., who had already extensively worked on achieving similar textures in silicon superstrates [24]. Based on their work, de Vrijer et al. worked on achieving the same at TU Delft using the following steps[25]:

- Growth of SiO_2 layer on the Si superstrate, using wet oxidation as a masking layer to protect the Si surface.
- Spin coating of a positive photoresist (referred to as PR) like SPR3012 onto the SiO_2 surface. The photoresist can be used to form the required pattern in the upcoming steps. This step also included a superstrate preparation step, where it is exposed to HMDS at 130^{o}C for 50 seconds to improve the hydrophobicity of the surface, as this aids in better adhesion of the PR to the superstrate.
- UV exposure of the PR-coated superstrate using a reticle, which has a scaled-down version of the pattern to be imprinted onto the PR.
- Development of the exposed parts in the PR, where the developer liquid dissolves these portions since they become soluble during the UV exposure step (in the case of a positive PR). Hard baking is also done after the development, to improve the resin bonding and the resistance to further processing steps like wet etching, dry etching, etc.

- Initial etching using Buffered Hydrofluoric acid (BHF), which contains 1 part HF mixed with 7 parts of NH4F, which helps to transfer the pattern from the PR into the SiO_2 masking layer. BHF is used as it has a controlled etching rate and hence forms the patterned SiO_2, without affecting the PR and without large effects of over-etching. This is followed by the removal of the PR layer using Acetone.
- The final etching step using poly-etch solution, where the HF interacts with the Si layer through the SiO_2 mask, thereby resulting in the formation of the honeycomb textures in the same, It is to be noted that the etch time here is an important parameter to be controlled to ensure that the textures are obtained with the required aspect ratio. Etching for lesser or longer durations can result in either no honeycombs being formed or a decrease in the aspect ratio of the honeycomb textures obtained.
- The remaining SiO_2 mask is finally removed using another etching step using HF.

These steps were modified and adopted to obtain the process steps required for creating honeycomb textures in glass superstrates. Since the superstrate used here is an alkaline aluminosilicate glass, which is already composed of SiO_2, the need for the formation of a masking layer is removed. Hence the steps associated with these have been removed. The basic process used for obtaining the honeycomb textures in the glass superstrates is depicted in the image 3.1 below:

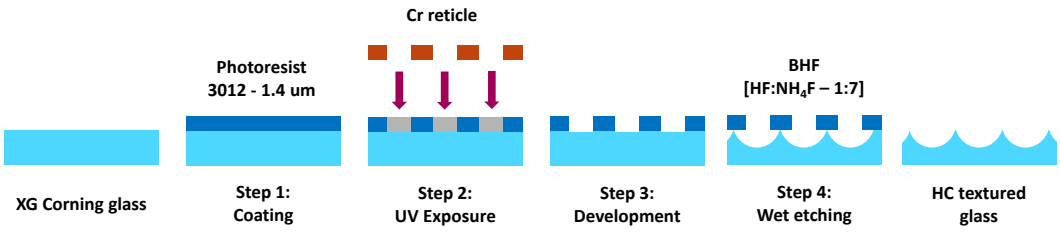

Figure 3.1: Flowchart for honeycomb texturing in glass superstrates

The individual steps present in the initial recipe that was devised for the hexagonal texturing of the glass superstrates are briefed in the following subsections.

3.1.1. Superstrate preparation

The first step in the process is to prepare the surface of the superstrate before the PR is coated. This is the most important step in the process, which has a direct effect on the uniformity and the strength of adhesion of the PR to the superstrate surface.

The superstrate used here is a Corning glass XG boro aluminosilicate glass wafer of 25mm in diameter

and 0.7mm in thickness with a primary flat. The primary flat is essential as it is used as an identifier during the alignment steps in various sub-processes of the photolithography process. The datasheet for the same is attached in appendix B.

Since the glass is mainly composed of silicon dioxide, it is extremely hydrophilic and has hydroxyl groups attached to the surface. As mentioned earlier in 2.5, it is essential for the surface to lose the hydroxyl groups for effective bonding of the PR to the surface. This required a basic cleaning step, to remove the impurities present on the surface. A pre-baking step was also considered as it could help to desorb the adsorbed hydroxyl groups on the surface. This could also promote the adhesion of the PR to the surface.

3.1.2. Coating of PR on superstrate

The next step involved coating the PR onto the glass superstrate. This was done in the EVG 120 coater machine in the Else Kooi Lab. This is an automated machine, which had a set of pre-designed recipes that could be loaded as per our application. The critical design parameters of the coating recipe are:

1. HMDS priming temperature and duration
2. Coater spin speed
3. Coater spin duration
4. Soft bake temperature and duration

The different recipes had different pre-set values for the above-mentioned parameters, depending upon the type of superstrate and photoresist being used. The coater spin speed and spin duration were mainly determined by the type of photoresist and the required thickness to be coated on the surface of the superstrate. The PR used in this recipe is SPZ 3012 and the available thickness values for this particular PR in the EVG120 are 1.4um and 2.1um. The TDS of the same is provided in appendix C. The HMDS priming duration was always done at 130^{o}C for 50 seconds, as this was standard for all recipes. Once the PR was coated onto the samples, they were soft-baked for 90 seconds at 90^{o}C. This was also kept constant for all recipes since this was the optimum for silicon-based superstrates.

3.1.3. Exposure of coated superstrates

Once the glass superstrates are coated with the required thickness of PR, the subsequent step involves the exposure of these superstrates. This is done using the ASML PAS5500/80 Waferstepper present in the EKL. A schematic representation of the various steps involved in the processing of the wafers in this equipment is shown in figure 3.2.

Before loading the wafers into the Waferstepper, the job type is chosen on the system intreface based on the processing required. A manual is provided next to the equipment for understanding the process parameters. The job type mainly depends upon the type of reticle being used and whether pre-alignment based on alignment markers is required before the exposure step.

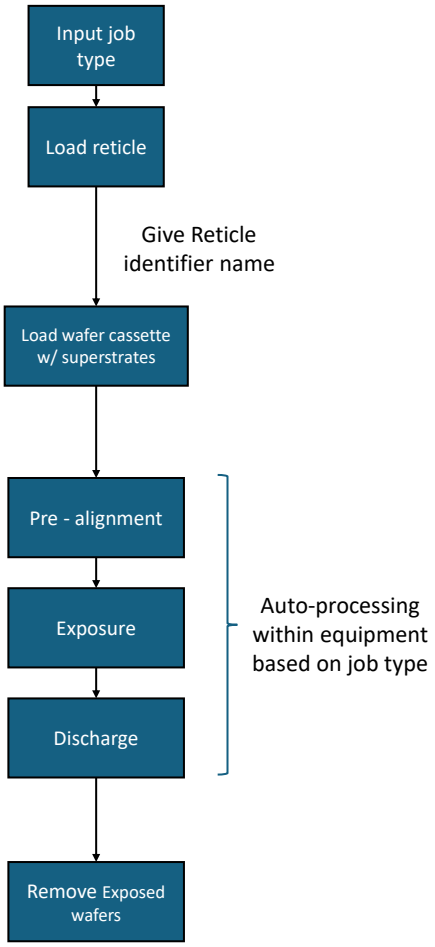

Figure 3.2: Flowchart - Exposure in PAS 5500/80 Stepper wafer

Since the glass wafers used here do not have any alignment markers, pre-alignment is not required. Hence the Diesize-10mm-n10a-1 job is to be chosen. It is to be noted that this job type is chosen since the reticle for the same is a single image reticle. However, when multi-image reticles are used, then the job type to be used depends upon the design of the reticle. This has been discussed in detail later in section 3.4.1.

The reticle is usually designed by downscaling the required pattern by a factor of 4 or 5 since the Wafer-stepper will magnify the image during exposure. The reticle used for obtaining the hexagonal textures is a pattern of holes spaced out at a particular periodicity along the horizontal and 60^o angle. This ensures that a honeycomb-shaped texture can be obtained when the superstrate with the patterned PR is etched, as shown in figure 3.3. The dimensioning of the reticle is done in such a way that, on exposure, the holes exposed in the PR will be at a periodicity of 3 μm with a hole dia of 1 μm each.

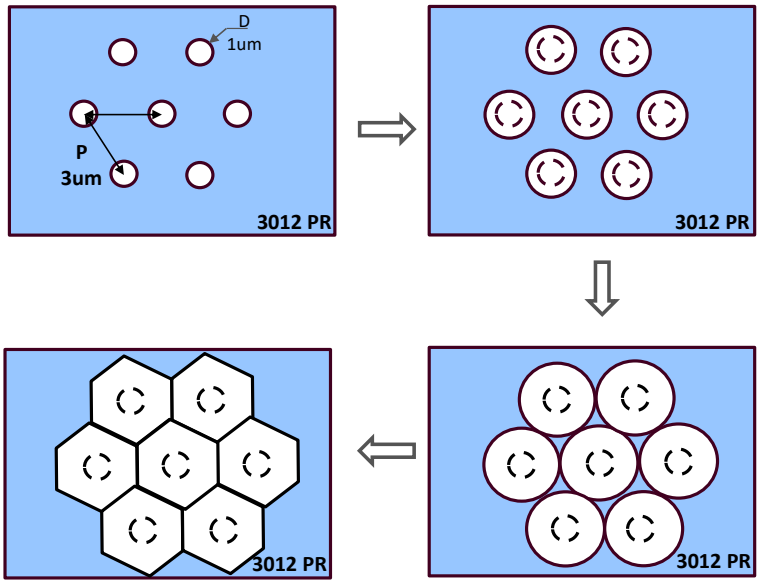

Figure 3.3: Formation of HC during etching

After entering the job type into the system, the reticle is to be loaded into the reticle carrier. Following this, the reticle carrier can be loaded into the equipment in the designated holders and the reticle name can be specified in the system. Since a single image reticle is used, the identified to be provided is A1. If a multi-image reticle is used, it should be 2X2 or 3X3, depending upon the matrix type the reticle belongs to.

Following this, the glass wafers are to be loaded into the wafer cassette. Here, it is to be noted that since the glass wafers being used lack alignment markers, the pre-alignment is done based on the position of the primary flat. Since the glass wafers are of a thickness of 0.7mm, the sensing of the primary flat poses an issue, causing the equipment to crash. This was overcome by using aluminum-based vacuum carrier wafers. These carrier wafers are 1 mm thick and are provided with a primary flat, which can help in easier alignment in the system. These carrier wafers are also provided with an airway pattern that provides a suction onto the base of the superstrate, thereby holding them in position. The usage of the carrier wafers also prevents the sagging of the wafers, thereby ensuring a uniform exposure dose across the entire surface of the PR. It is important while loading to ensure that the primary flat of the carrier wafers and the glass wafers are aligned manually, before loading them into the equipment.

The exposure dose is determined based on the thickness of the PR used. For 1.4um thickness, a dosage of 150 MJ is preferred, while for a thickness of 2.1um, the dosage to be used is 315 MJ. Once all these parameters are fixed and the reticle and the wafers are loaded, the job can be started. The wafers are then transferred through three stages by the wafer arm, as shown in figure 3.2. The wafers are aligned based on the primary flat position and then sent to the exposure chuck. Here the wafers are exposed to UV light of the specified power dosage, through the particular reticular image that was selected in the job description. The exposure process can be virtually followed on the interface provided along with the equipment. Once the exposure is completed, the exposed wafer is moved to the discharge chuck. From here, the wafer arm moves

the exposed wafers and the carrier wafer to the cassette in the output port.

3.1.4. Development of Exposed superstrates

This is the final step of the photolithography process in which the exposed superstrates are developed in the EVG120 Developer. There are multiple recipes offered in the EVG120, but in this project, the standard single puddle recipe, indicated by 1-Dev-SP was used. In this recipe, the superstrate is shifted to the developer rack, where the superstrate is spun at 5 rpm, while the developer solution is poured onto the surface. The slow spin speed ensures a uniform layer of the developer solution, which reacts with the exposed parts of the PR and dissolves them. Following this, the superstrate is allowed to spin at high speeds ranging from 2000 to 3000 rpm and washed with DI water, ensuring that the dissolved PR is removed from the surface. Following this, the superstrate with the developed pattern is then baked at 100^{o}C for 90 seconds, to evaporate excess PR and developer present on the superstrate.

Finally, the superstrate with the patterned PR was obtained. The image of the same when viewed under a microscope at 50X magnification is shown below in figure 3.4.

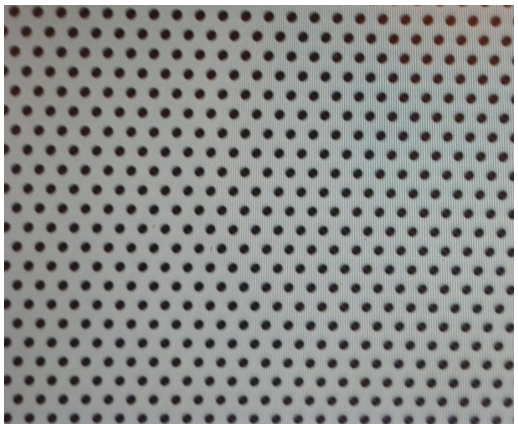

Figure 3.4: PR of hole dia 1 μm and periodicity 3 μm

3.1.5. Wet etching of patterned superstrates

Now, the glass superstrate with the patterned PR is to be chemically etched, to obtain the hexagonal texturing on the surface. This is done in a sequence of two steps. The first step involves a 1-minute dip in a 1:5000 aqueous Triton X-100 bath. The main purpose of this bath is to improve the wettability of the surface by the etchant. The triton x-100 can do this as it acts as a surfactant, lowering the surface tension and enabling better contact between the solid and the aqueous medium [27]. Following this, the wafer is dipped in an etchant bath composed of BOE (Buffered Oxide Etch) 7:1. This solution is a pre-made solution of BHF (Buffered Hydrofluoric acid) comprised of the following mix of chemicals:

- 87.5 wt % Ammonium Fluoride (NH4F) (40%)
- 12.5 wt % Hydrofluoric acid (HF) (49%)
- Water

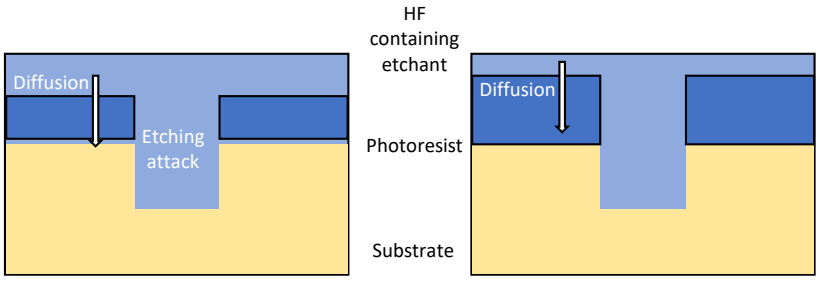

Figure 3.5: Peeling off of PR due to diffusion of F- ions through PR

For glass etching, the preferred etchant is Hydrofluoric acid (HF) as it offers a high etching rate of around 833 nm/min at 40 % concentration. However, the usage of HF increases the peeling off of the PR due to the influx of the F- ions through the PR, as shown in figure 3.5 [28] [29].

However, when HF is mixed with BHF, the buffer results in an increase in the concentration of F- ions and these ions, due to their high electronegativity, tend to form HF_2- ions. The PR is more resistant to the diffusion of these ions, owing to their larger size. This helps to protect the PR from the impact of HF, while also achieving the objective of etching the glass [28] [30].

The etching time for the same was determined by carrying out a time series experiment, ranging from 18 minutes to 30 minutes. It is to be noted that the wafers were etched individually, as previous work showed that etching multiple wafers together affected the etching process due to the deposition of the peeled-off PR onto other wafers [21].

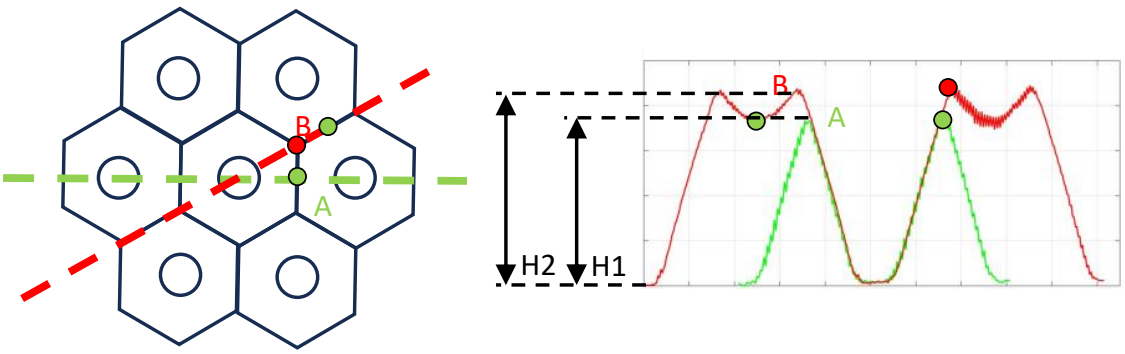

Figure 3.6: G and R axis in honeycomb textures (left) and the section profile along the G and R axes (right)

While characterizing the periodic textures, it was observed that the parameters differed along two axes, with a phase difference of 30^o. This occurred due to the variation in the gap between the holes in the photoresist, which varies cyclically, repeating every 60^o. The axis along the center of the holes is taken as the green axis (G), while the axis along the edges of the honeycombs is taken as the red axis (R). In figure 3.6 the distance of point A from the hole would be around P/2, while for point B, the distance would be P/$\sqrt{3}$. Since, B is farther from the hole than A, the height at B can be expected to be higher than A.

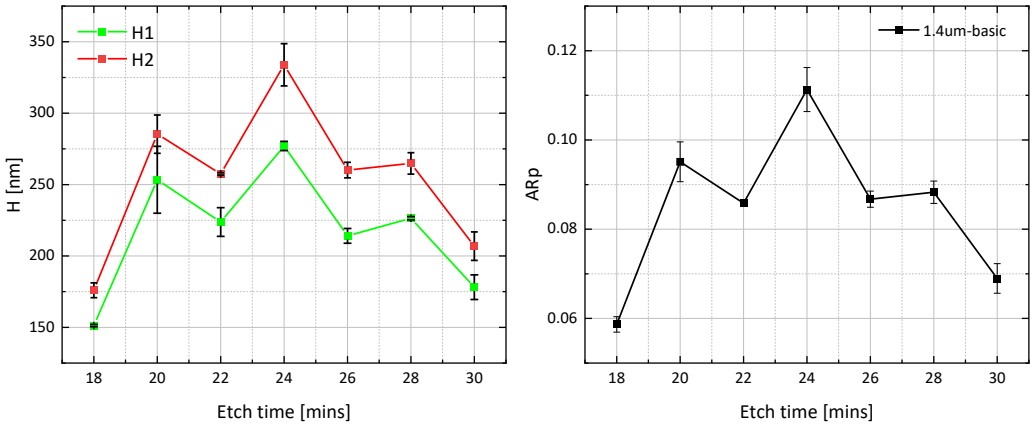

Figure 3.7: G axis and R axis Texture height variation with etch time (left); ARp variation with etch time (right)

The figure 3.7 shows the variation of the texture height along the G and R axes with etch time. It can be seen that the maximum texture height of 330 nm was achieved after 24 minutes of etching. The graph on the right in figure 3.7 shows the variation of the ARp with etch time. Thus, the maximum ARp that could be achieved in the hexagonal textured glass, using the above-mentioned recipe was 0.11.

3.2. Equivalent hole radius (Re)

The equivalent hole radius is a parameter that can be used to understand the quality of the texturing process. Thierry et al. devised the formula shown in 3.1 which relates the hole radius (r), periodicity of the pattern (p) and the expected texture height (h)[25]. According to this formula, when the PR pattern with a hole dia 1μm and periodicity 3 μm is used, the deepest texture height that must be obtained should be around 1.23 μm. This would result in an ARp of 0.41.

$$r = \frac{P}{\sqrt{3}} - H \tag{3.1}$$

Now, if we calculate the equivalent hole radius from the actual maximum texture height obtained (330 nm), with the same periodicity of 3 μm, the resulting value is around 1.4 μm. The equivalent hole radius indicates the actual hole radius that, in an ideal case where there is no PR peel-off, would achieve the same texture height for the particular periodicity. This implies that during the wet etching process, the hole diameter does

not stay constant at 1 μm, but increases as the etching continues. As the hole dia increases, the impact of the etchant on the glass close to the glass-PR interface increases, as a result of which the etching at the peaks of the honeycomb becomes faster. This continues till a particular critical level of PR peel-off, beyond which the etching at the peak occurs at a larger rate than at the bottom, resulting in a drop in the texture height. Thus, the maximum texture height is mainly dependent on the extent of peel-off occurring in the PR.

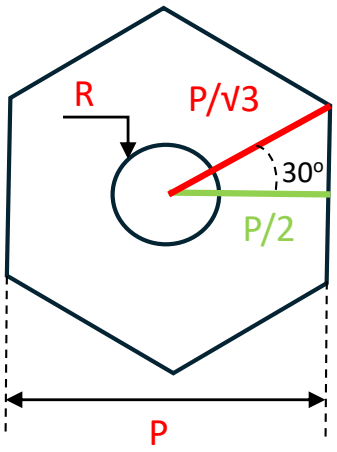

Figure 3.8: Schematic representation of the dimensions of a honeycomb

The PR peel-off is mainly determined by the adhesion of the PR to the glass surface. An improvement in the adhesion would result in a decrease in the Re and an increase in texture height. To control this peel-off rate, it is essential to understand how the different processes in the photolithography process affect the PR adhesion and texturing process. This is looked into further in the section 3.3.

3.3. Impact of photolithography steps on texture

In this section, different individual steps in the photolithography were studied and their effect on the texturing process was understood. The choice of these steps was done heuristically as along with the aforementioned objective, another important goal was to understand how the texturing process could be modified to obtain deep hexagonal textures in the glass. When observing the texturing steps mentioned in section 3.1, it was noted that peeling off of the PR occurred during the wet etching step. Literature shows that this peel-off occurs mainly when the adhesion of the PR to the superstrate surface is poor [28].

Thus, it was essential to choose parameters that could have a direct impact on this property.

3.3.1. Influence of cleaning method

It was observed that the uniformity of the texture across the surface and the efficient adhesion of the PR to the glass surface are influenced by the cleaning step done before the processing of the samples. The first option for this was to use a handmade bath of acetone and Isopropanol (IPA) since these solutions could help in the removal of the organic impurities. The sample would be dipped in Acetone for 5 mins. Following this, it would be shifted to an IPA bath for 5 minutes. It was necessary to dip the sample in IPA immediately after the acetone bath to prevent streaking on the glass. The samples were cleaned using this step and then processed using the methodology mentioned in section 3.1. However, post-etching, it was seen that the texturing process was non-uniform across the entire surface, resulting in certain parts of the superstrate being etched while the other portions remained unetched.

It is to be noted that a similar response was obtained when the processing was done without prior cleaning of the sample. This indicates that the cleaning with Acetone and IPA is not enough to remove the presence of impurities completely. Following this, the next option considered was the standard cleaning available in the EKL. This consisted of the following steps:

1. Dip the wafers in 99% Nitric acid (HNO_3) for 5 minutes. The main objective for this is to remove the organic impurities present on the sample.
2. Clean the samples in a DI rinse bath for 5 minutes.
3. Dip the wafers in 69.5 % HNO_3 for 5 minutes. This was meant to remove any inorganic impurities present on the sample.
4. Clean the samples in a DI rinse bath for 5 minutes.
5. Dry the samples by using the standard 8-minute program in the spin dryer. This is used to remove the moisture from the cleaned samples.

In addition to this, it was discovered from the literature that the concentration of nitric acid has an impact on the surface of the corning glass, texturing the surface and also varying the chemical composition of the glass[31]. As a result, three more handmade baths of HNO_3 of varying concentrations were considered individually, viz. 99% HNO_3, 69.5% HNO_3 and 30% HNO_3. The cleaning using these baths was done by dipping the samples in them for 3 mins followed by dipping them in a running water bath for 5 mins. Post this, the samples were dried by using the dryer, as mentioned in step 5 in the cleaning line option.

The effect of these cleaning steps was compared by etching all the samples for 20 minutes using the wet etching methodology, mentioned in 3.1.5. Following this, the profile measurement was done and the texture height obtained along the G and R axes have been shown in the graph 3.9 below.

Here, it is to be noted that the texture height increase for the subsequent cleaning methods when being etched for the same time implies that the strength of adhesion between the PR and the glass is being impacted positively. This is because as mentioned in section 2.8, the PR helps in forming the hexagonal texture by allowing the downward etching to be faster at the bottom of the texture than at the peak. An increase in the texture height for the same etch duration will occur only when this difference increases, implying that the

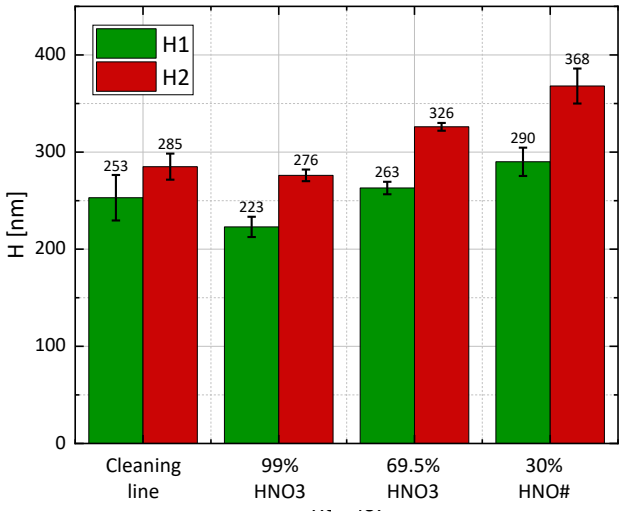

Figure 3.9: Comparison of texture height of different cleaning methodologies; 1 - Cleaning line, 2 - 99% HNO_3, 3 - 69.5% HNO_3, 4 - 30% HNO_3

etching at the peak is reduced. This can occur as a result of a reduction in the peel-off of the PR. This would imply that the cleaning methodology based on the 30% HNO_3 has the best adhesive nature resulting in the deepest textures.

However, when we consider the standard deviation of the height measurement done at various points on the sample, it can be seen that it is the lowest at 10nm for the cleaning methodology utilizing the 69.5% handmade HNO_3 bath. Also, in the case of the 30% HNO_3 bath, the SD increases to 40 nm, which is comparable to that of the cleaning line step, around 45 nm. This implies that though the adhesion is better for the 30% HNO_3 cleaning, the uniformity of the adhesion across the entire surface drops. Thus, the cleaning step utilizing the 69.5% HNO_3 handmade bath was taken as the optimum choice.

3.3.2. Measuring Hydrophobicity of surfaces

It has been stated already that the adhesion between the PR and the superstrate surface in the photolithography process has an impact on the texture height by effect of the etching rate. This adhesion is negatively affected by the presence of water or moisture on the surface, before the coating step. As mentioned earlier in 2.5, this is because the presence of moisture leads to an increase in the polar bonding on the surface, which inhibits the PR from bonding with the surface of the superstrate. The presence of moisture is linked to the hydrophobicity of the surface, which implies the tendency of the surface to repel bonding with water molecules. The surface energy or the hydrophobicity of the surface could be related to the contact angle of a water droplet dropped onto the surface. This could be measured from the WCA (water contact angle), the contact angle formed by a water droplet on the surface of the superstrate. This was done using the Dataphysics contact angle system OCA20, available in the EKL CR100. A drawing model of the same is shown in figure 3.10 below.

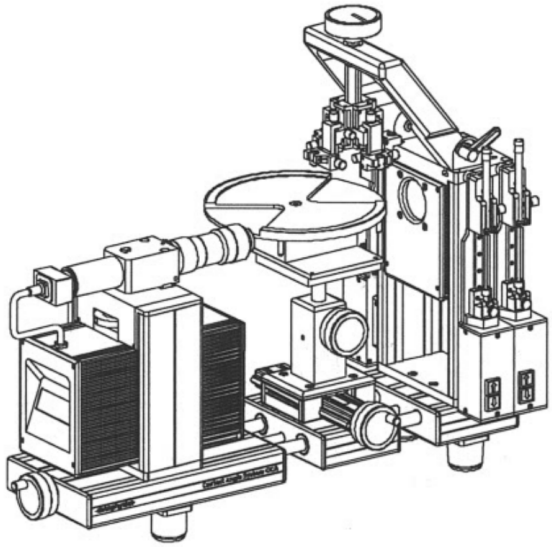

Figure 3.10: Drawing model of Dataphysics OCA20

1 ul of water was dropped on 5 different spots on the superstrate and a microscopic image of the droplet profile on the superstrate was captured. Following this, the droplet's left and right contact angle with the superstrate was calculated using the software. The mean of the five values was used as an indication of the hydrophobicity of the surface, which in turn could be related to the adhesiveness of the surface with the photoresist, as shown in the image 3.11 below.

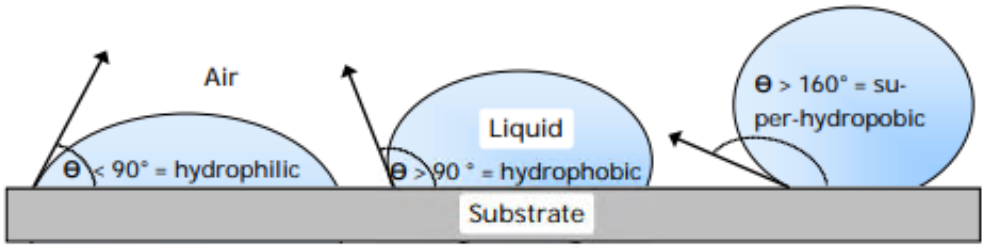

Figure 3.11: Relationship between contact angle and hydrophobicity of surface [32]

If the surface has low surface energy or low hydrophobicity, then the contact angle would be lesser as the water droplet would be pulled more by the surface. However, when the surface has a high surface energy of high hydrophobicity, the contact angle will be higher as the water droplet will be repelled away from the surface [33] [32]. Thus, for the following processes, the influence of the water contact angle is studied. This gave us an idea of how the process would affect the PR adhesion and thereby, indicate the effect on the texturing process.

3.3.3. Influence of Pre-bake temperature

The next step to be studied is the pre-baking of samples before the actual photolithography process. As mentioned earlier in section 2.5, dehydrating the sample helps to achieve a better PR adhesion to the surface. One way to achieve this is by pre-baking, i.e. heating the superstrate before coating the PR on them. The maximum duration for the pre-baking was fixed at 10 minutes since the dipod arm in the EVG120 could not handle hot superstrates. If the superstrates were to be heated for a longer duration, they had to be cooled again before being used in the EVG120. This delay could offer enough time for the surface to re-adsorb water.

The pre-baking was done by heating the samples in the Memmert oven present in the EKL. The Memmert oven has an operating range of 90^{o}C to 200^{o}C. To determine the optimum pre-bake temperature, the samples were heated at different temperatures ranging from 100^{o}C to 140^{o}C, in steps of 10^{o}C. This temperature range was suggested by the manual provided by Microchemicals for sample preparation [34]. After the pre-baking step, the samples were primed with HMDS for 50 seconds at 130^{o}C. The WCA of these samples was then measured using the OCA which is indicated in the graph 3.12 below.

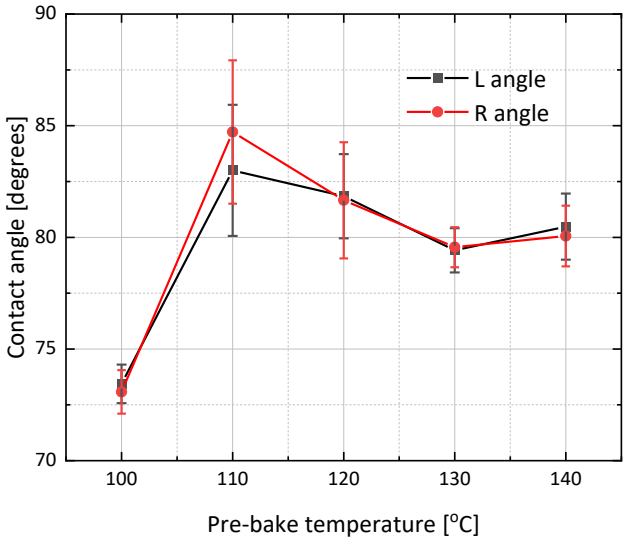

Figure 3.12: Comparison of mean WCA of different PBT

It can be seen that the mean WCA peaks around 85^o for the samples that were pre-baked at a temperature of 110^{o}C. Hence, this temperature of 110^{o}C was chosen as the optimum pre-bake temperature for the samples, which was to be done before they were coated with the PR.

3.3.4. Influence of HMDS exposure duration

Another important process that helps in optimizing the PR adhesion is the HMDS priming of the surface before coating. [10] The provision for this is provided in the EVG120. The equipment has a separate priming chamber, where the samples are exposed to HMDS along with N2 as the carrier gas. The exposure duration

range offered by the equipment was 50 seconds to 150 seconds, at a temperature of 130^{o}C. To determine the effect of the exposure duration on the PR adhesion, the samples were cleaned using the 69.5% HNO_3 bath, as mentioned in 3.3.1 and then primed with HMDS for different periods, from 50 to 150 seconds, in steps of 50 seconds. The WCA of these samples was then measured, which is depicted in the plot 3.13 below.

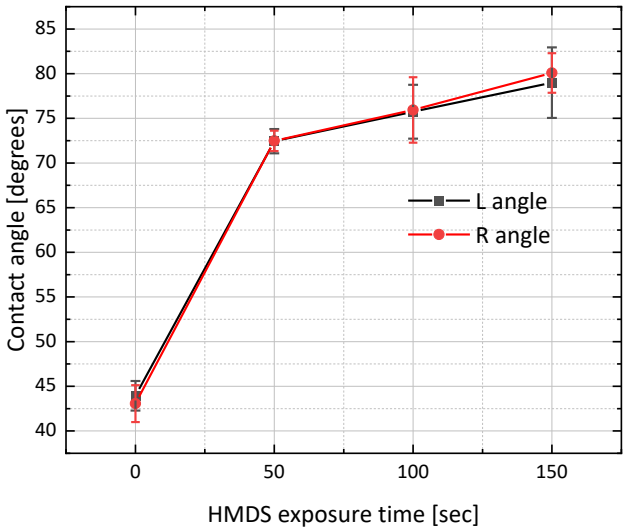

Figure 3.13: Comparison of mean WCA of different HMDS exposure durations

It is to be noted that the zero value of the exposure duration in figure 3.13 indicates WCA of the sample surface right after the cleaning step without any HMDS priming. This was around 45^o, indicating the hydrophilicity of the surface before HMDS priming. However, the WCA increases with increased exposure duration of HMDS, peaking at 80 ^{o} for 150 seconds. This can be explained as the result of the greater presence of the non-polar trimethylsilyl groups on the glass surface, with increased duration of HMDS priming[12][11]. The reaction for the same is shown in figure 2.6 in section 2.5.

3.3.5. Influence of coating parameters

Film thickness	2000 rpm	3000 rpm	4000 rpm	5000 rpm
Mean [μm]	1.61	1.31	1.13	1.02
STD Dev [nm]	1.2	0.8	0.5	1.1

Table 3.1: Film thickness of AZ ECI 3012PR obtained at different coater spin speed [35]

The main parameters of the coating process that influence the PR characteristics are the coating speed and coating duration. These parameters are mainly determined by the type of the PR being used. The thickness of the PR layer to be formed on the surface mainly determines the spin speed at which the coating is done.

The PR used in the EVG 120 is AZ ECI 3012 from Merck. Figure 3.14 shows the spin speed to be maintained for acquiring different thicknesses of the PR.

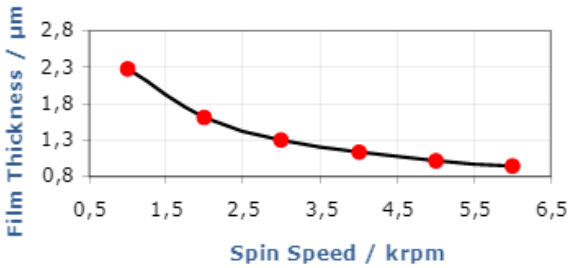

Figure 3.14: Spin curve of AZ ECI 3012 PR [35]

The thickness options in the EVG120 for the 3012 PR were 1.4um and 2.1um. Based on the table 3.1 provided in the datasheet offered by Merck. the spin speeds of the coater for obtaining these thicknesses were 3000 rpm and 2500 rpm respectively. The overall coating duration was around 30 seconds. These recipes were not provided with an EBR (Edge bead removal) step. These parameters were kept the same for almost all the recipes since the thickness of the PR was set as a standard parameter [35].

3.3.6. Influence of soft bake duration

Following coating of the PR, it was essential to heat the coated superstrate in order to remove the excess PR from the surface. This is called soft baking and ensures that a monolayer of the PR is formed on the superstrate surface. The objective of this experiment was to understand the effect of the soft-bake duration on the hydrophobicity of the superstrate surface. The monolayer ensures that the accuracy of the pattern is maintained post-development, enabling the formation of a precise PR mask on the superstrate. In the standard recipe, the soft bake in the EVG120 was done at a temperature of 90^{o}C for 90 seconds in a dedicated chamber, since this was the optimum suggested in the Technical Datasheet (TDS) offered by Merck [35]. Since the parameters associated with this chamber were always kept constant, it was decided to use the same parameters for all our samples as well.

However, to understand the effect of the soft bake duration, post coating the samples were soft baked separately at 90^{o}C in the Memmert oven within a range of 60 to 120 seconds, in steps of 20 seconds. Similar to the previous experiments, the hydrophobicity of these superstrates was also measured using the WCA (Water Contact Angle), as described earlier in section 3.3.2. From figure 3.15, it is evident that the hydrophobicity would improve by increasing the soft bake duration to 100 seconds. However, the duration was not changed and the standard parameter was used for all the samples.

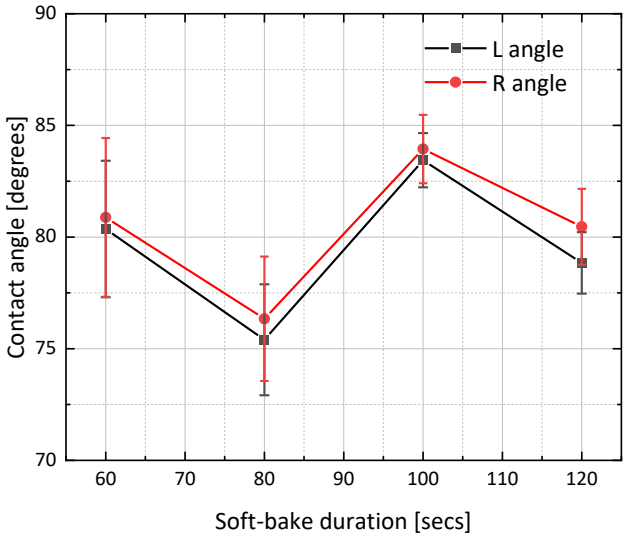

Figure 3.15: Comparison of mean WCA of different Soft bake durations

3.3.7. Influence of Hard bake parameters

The final step associated with the photolithography process, that was analyzed was the hard baking of the superstrates post-development. Hard baking is generally done to physically and chemically stabilize the PR material. This stabilization can also be done by exposing the PR to low-UV radiation. However, we have chosen the simpler step of heating the samples at particular temperatures, depending on the type of PR being used.

The effect induced by the hard baking step depends mainly on the temperature at which the superstrates are hard-baked. In general, the hard baking of the developed superstrate at the reflow temperature, results in a process called ”roundening” [34] [36]. In this, the PR softens and the upper surfaces of the PR begin to rounden due to the evaporation of the PR from these parts. However, at the interface of the PR with the superstrate, the PR remains. This can be seen in the figure 3.16 below, which shows a top-view image of the developed PR, after hard baking. In comparison to the PR shown in figure 3.4, it can be seen that after hard baking. the holes at the top surface of the PR have become larger due to the roundening effect. This effect does not majorly affect the wet etching process and hence can be tolerated.

Two different hard baking procedures were selected to visualize the effect of the hard baking on the PR adhesion. The first option was a two-step process, which was a standard photolithography process being followed by the EKL team. The first step, referred to as HB110, involved heating the superstrates at 110^{o}C for 30 minutes, followed by the second step in which the superstrates were heated at 130^{o}C for another 30 minutes. The second option involved hard baking the superstrates by heating them at 140^{o}C for 30 minutes which was referred to as HB140. This option was chosen specifically to understand the effect of baking the developed superstrates at a temperature higher than the reflow temperature of the PR[36]. Hard baking

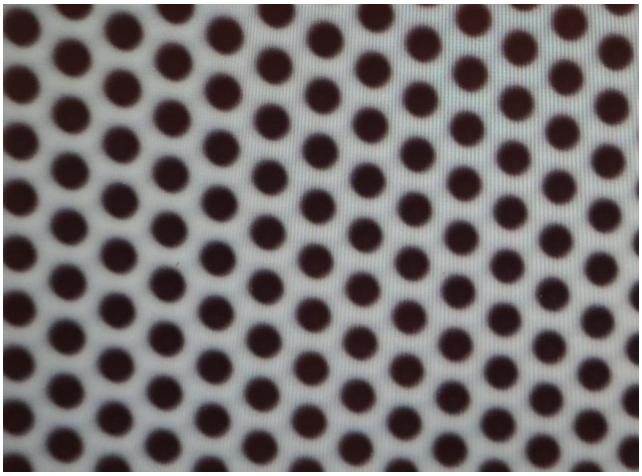

Figure 3.16: Roundening of PR after hard baking at 140^{o}C for 30 minutes

of the samples at such temperatures could result in a thermal cross-linking of the PR[37]. This could, in turn, improve the PR stability against wet etching and thereby improve the depth of the textures that could be obtained. However, hard baking at such high temperatures can also result in crack formation in the PR, which could allow the etchant to seep in during the wet etching process, thereby affecting the uniformity of the textures[36]. This was prevented by allowing the hard-baked superstrates to cool down by placing them at room temperature for 5 minutes immediately after hard baking. To visualize the effect of the hard baking experiment, it was necessary to etch the samples as well. Since the hard baking was done after the development process, the WCA could not be an indicative parameter of the adhesion promotion. Thus, the samples were etched using the etching procedure mentioned in section 3.1.5 for a time range of 18 to 30 minutes. These samples were cleaned using the methodology mentioned in 3.3.1, while the other parameters were kept the same as in the basic recipe, provided in 2.5. The left graph in the figure 3.17 below indicates the texture height along the G and R axes obtained at different etch times for the different hard bake conditions.

The first thing to be noticed is that the maximum texture height has been obtained at an etch time of 18 minutes in both the hard bake conditions. It is also evident that the hard bake step at 140 ^{0}C results in a deeper texture height than the other hard bake step at all etch times. The equivalent hole radius obtained for the HB110 and HB140 steps are 1.36 μm and 1.27 μm respectively. The drop in the equivalent hole radius implies that the texturing at the maximum height is getting closer to the ideal case where no PR peel-off occurs. This in turn implies that the cross-linking of the PR has improved the adhesion of the PR to the superstrate. It was also visually observed that the peel-off occurred in a more reduced manner in the case, in comparison to the samples hard baked at 110^{o}C. On observing the ARp variation in the graph on the right in figure 3.17, the maximum ARp of 0.15 was obtained when the sample was etched for 18 minutes after hard baking at 140^{o}C for 30 minutes. Thus, this hard bake step was taken as the optimum step for developing the optimized recipe later.

Since the peaking of the texture height and ARp occurred at the lower limit of 18 minutes, the range of the etch time for the better hard baking parameter was extended to 14 minutes. However, it was observed that

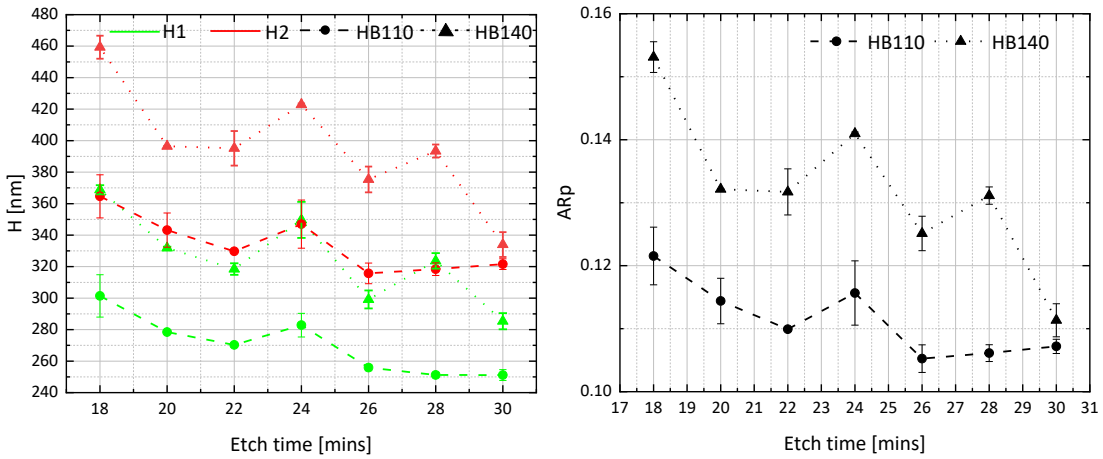

Figure 3.17: G and R axes texture height variation with time for HB110 and HB140 (left); ARp variation with time for HB110 and HB140

these were lower than the 18-minute texture height. This is shown in figure 3.20 later in the following section.

3.4. Design of new recipe

Based on the analysis of the different steps done in 3.3, an optimized recipe was developed, as shown in figure 3.19 below.

In addition to the steps mentioned in 3.1, the following steps have been added or modified to develop the optimized recipe.

1. Cleaning of samples in a bath of 69.5% HNO_3 for 3 minutes followed by a dip in running water bath for 5 minutes. The samples are then dried by using the standard 8-minute program in the spin dryer.
2. Pre-baking of the samples at 110^{o}C for 10 minutes in the Memmert oven.
3. HMDS priming prior to coating at 150^{o}C for 150 seconds. Here, the priming was chosen to be done at an elevated temperature of 150^{o}C, since the work done by Chodkowski et al. showed that an increased temperature helped in faster replacement of the hydroxyl groups by the trimethylsilyl groups [12]. Unfortunately, there were no recipes pre-loaded in the EVG120 for trying out the influence of the same, before incorporating the same in the optimized recipe.

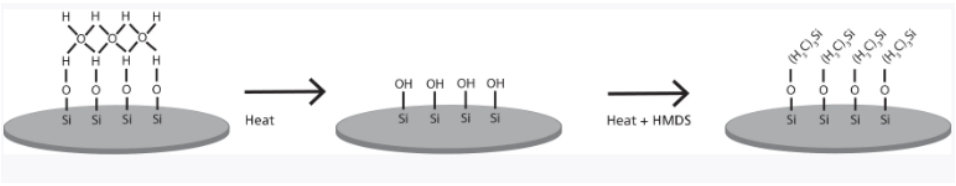

Figure 3.18: Effect of HMDS priming at higher temperature [12]

4. Hard baking of samples post-development for 30 minutes at 140 ^{o}C for 30 minutes in the Memmert oven.

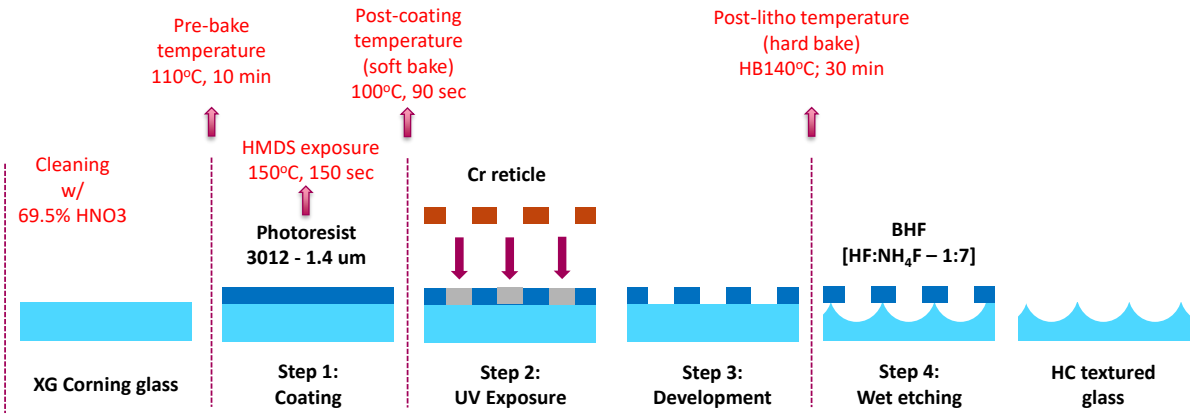

Figure 3.19: Recipe with optimized parameters for enhanced adhesion of PR

The samples prepared using the optimized recipe were etched for a time series, ranging from 14 minutes to 24 minutes. Here, the thickness of the PR was varied to understand the influence of the same. This is because theoretically, a thicker PR should lead to deeper textures since the increase in thickness further reduces the influx of the etchant ions through the PR. The G and R texture height variation is shown in the left in the figure 3.20 below.

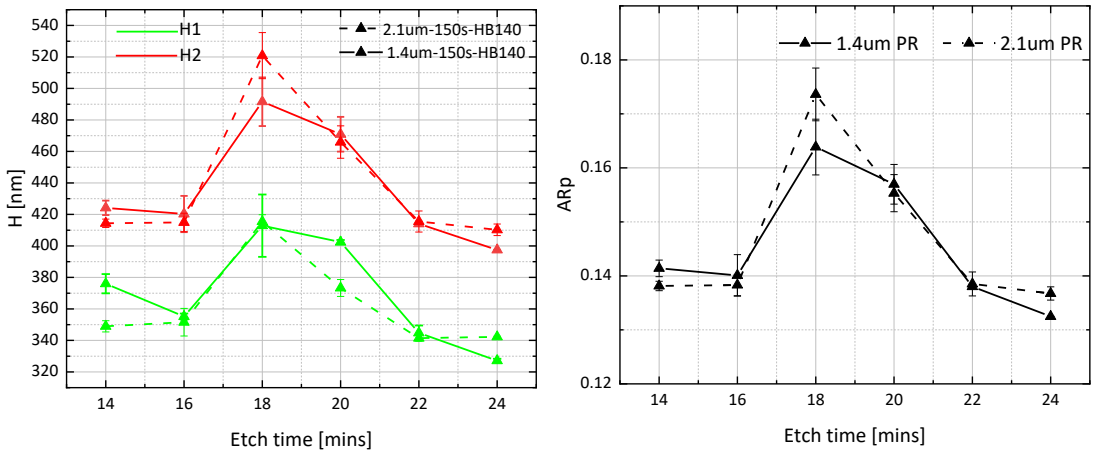

Figure 3.20: G and R axes texture height variation (left) and ARp variation (right) with time for 1.4um and 2.1um PR thickness using optimised recipe

It can be seen that the maximum texture height has been obtained in both cases for an etch duration of 18 minutes. In addition, it can be seen that the height for the 1.4um PR curve is almost the same at all etch times other than the 18-minute peak. This is because the PR peel-off starts occurring between the 16 and 18-minute

duration and due to improved adhesion of the 2.1um PR, the peel-off is slower for the latter. The equation 3.1 can be used to calculate the equivalent hole radius that the PR must have to obtain these heights [25]. Since the periodicity is the same, the difference in the equivalent hole radii will be the same as the difference in the texture height. The reduction in the equivalent hole radius obtained after etching for the same time implies that the peel-off has a lesser impact on the thicker PR. This could be explained as a result of the reduced diffusion of the etchant ions through the PR of increased thickness. Thus, after etching for around 18 minutes with the thicker PR of 2.1 μm, the maximum texture height of 520 nm is achieved along the R axis. However, once the PR peel-off occurs, the etching continues at the same rate for both the PR thicknesses, indicated by the overlapping of the curves at all other etch times. Thus, the deepest ARp that could be obtained using the reticle of hole dia 1 μm and Periodicity 3 μm is 0.17 after etching for 18 minutes.

3.4.1. Influence of Periodicity

In addition to the influence of the different processes in photolithography, the influence of the reticle design on the texturing process was also studied. The alternate reticle designs were available in a 2X2 reticle, designated as PVMD-hex. The parameters of these patterns that were available for usage in the texturing process are shown below in table 3.2.

Mask ID	Stepperwafer Tag	Hole dia [μm]	Hole Periodicity [μm]
PVMD-hex-BL	Image-1	1	4
PVMD-hex-BR	Image-2	1	5
PVMD-hex-TL	Image-3	0.6	4
PVMD-hex-TR	Image-4	0.6	5

Table 3.2: Design parameters of reticle PVMD-hex

The diagrammatic representation of the 2x2 reticle is shown below in figure 3.21. When this reticle is being used in the stepper wafer, it is necessary to set the reticle identifier as 2X2. Following this, the program must be directed to use any one image from the reticle, by calling the appropriate tag, as mentioned in table 3.2. The PR thickness used for this experiment was 2.1 μm and hence the exposure dose was to be increased to 315 MJ. The optimized recipe mentioned in section 3.4 was used for the production of these superstrates.

While processing, it was noted that for the superstrates made using the reticle design with hole dia as 0.6 μm, the pattern was not replicated onto the PR in the superstrate. This was because the hole diameter of 0.6 μm was too close to the tolerance limit of the exposure system, as a result of which the holes were not formed during the exposure process. Hence, the superstrates could be produced using only the first two images of the reticle design, shown in the table 3.2. Thus, only the effect of periodicity on the texturing process could be studied.

The samples made using the two reticle designs of D1P4 and D1P5 were then etched for a time series ranging from 14 to 24 minutes. The graph below in figure 3.22 shows the ARp on the left, obtained after etching for different times, ranging from 14 to 24 minutes, for the 3 reticle designs, D1P3, D1P4 and D1P5.

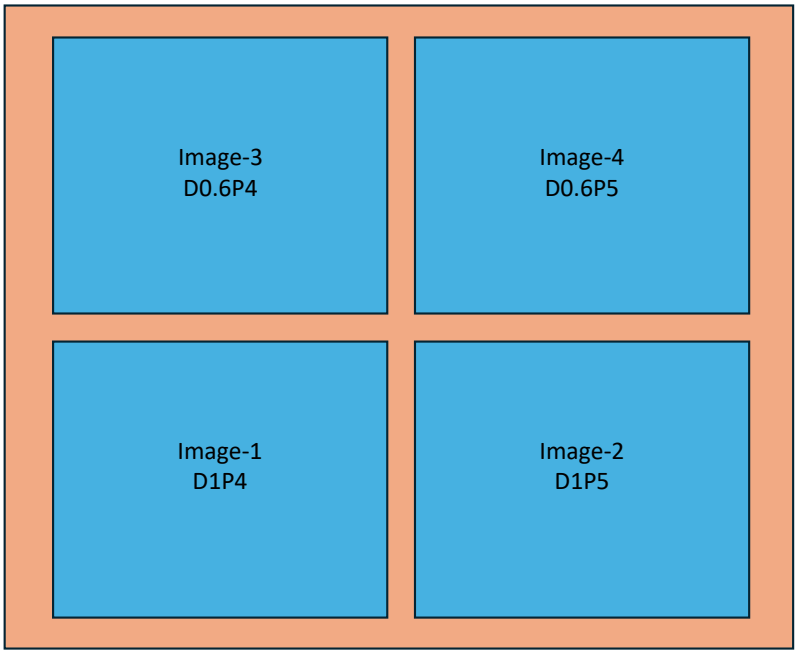

Figure 3.21: Pictorial representation of design pattern in PVMD-hex reticle

The improvement in adhesion can be visualized from the height variation shown on the left in figure 3.22. It is to be noted that the peak in the texture heights has shifted from 18-minute etching to 20-minute etching for the samples with increased periodicity. The drop in the red axis height occurs only after 20 minutes in the case of the P4 and P5 curves, while the drop occurs at around 18 minutes for the P3 curve.

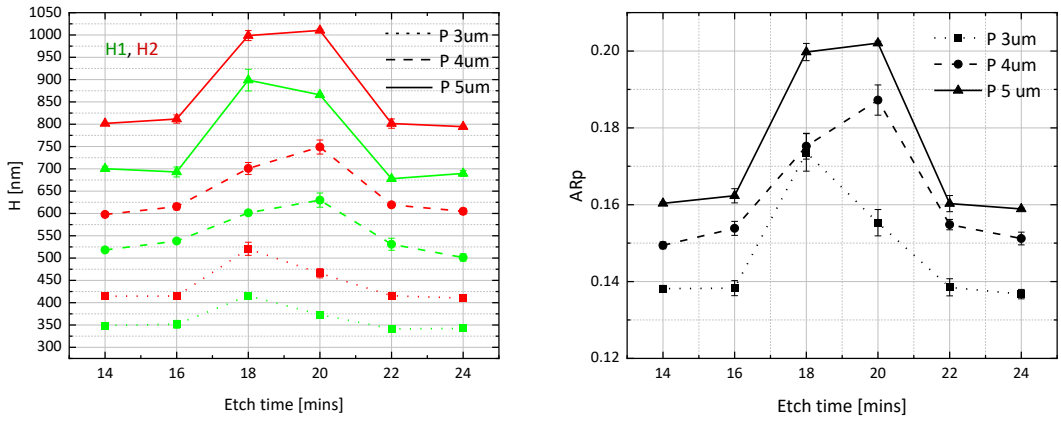

Figure 3.22: ARp variation with etch time for reticle design of different periodicity

Hole dia [μm]	Hole Periodicity [μm]	Expected height [μm]	Expected ARp	Actual height [μm]	Actual ARp
1	3	0.73	0.24	0.52	0.17
1	4	1.31	0.33	0.75	0.19
1	5	1.88	0.38	1	0.2

Table 3.3: Expected and actual values of H and ARp for different periodicities

Using the equation 3.1 [25], the expected maximum texture height that can be obtained by using these masks is shown in table 3.3. The equivalent hole radii that would result in these actual texture heights in an ideal situation are calculated to be 1.21, 1.56, and 1.89 μm respectively.

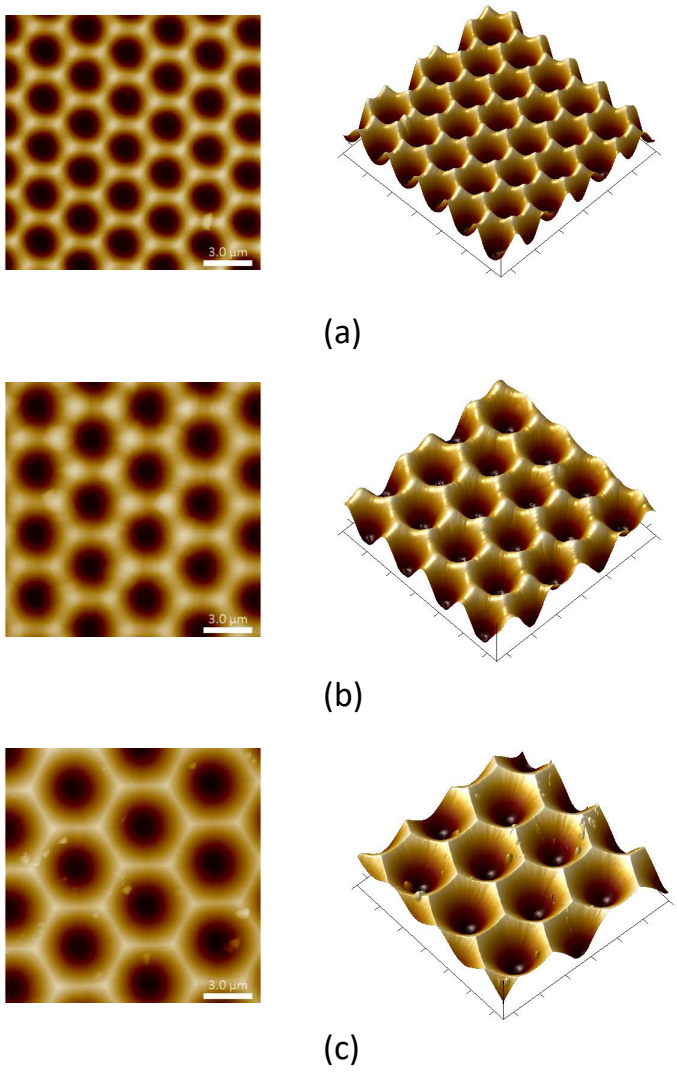

Figure 3.23: 2D (left) and 3D (right) AFM measurement of honeycomb textured samples with P of 3μm, 4μm and 5μm (from top to bottom)

3.5. Influence of different parameters on Equivalent hole radius Re

To understand the effect of the different processes, a comparison between the different parameters and the resulting texture height and equivalent hole radius values are drafted. This is shown in the table 3.4 below. Using the equation 3.1, the ARp of a hexagonal texture in an ideal case can be depicted as shown in equation 3.2, where r is the hole radius and P is the periodicity of the pattern.

$$ARp = \frac{1}{\sqrt{3}} - \frac{r}{P} \tag{3.2}$$

However, we noticed that the actual ARp does not conform with this equation and can be obtained by replacing r with the equivalent hole radius Re. This is a result of the peeling off of the PR which results in a drop in the texture height obtained. This peeling off can be represented by using the equivalent hole radius, Re. As mentioned earlier in section 3.2 this parameter indicates the hole radius that the pattern must have had for it to produce the obtained texture height, in an ideal etching scenario without any PR peel-off. Now, from the equivalent hole radius and the Re/P values shown in the table 3.4 below, it is clear that the parameters taken up in the optimized recipe have resulted in a decrease of the same. This implies that these parameters have improved the quality of the adhesion between the PR and the glass, thereby enabling deeper texture heights for the same periodicity.

As the periodicity is increased, it can be seen that the Re/P ratio further decreases. These hexagonal textures were made using the reticle dimensions of D 1 μm and periodicities 3 μm, 4 μm and 5 μm. These would have an r/P ratio of 0.17, 0.13 and 0.1 respectively. However, the corresponding Re/P values are 0.4, 0.39 and 0.38. This implies that the improvement in the P does not play a major role in promoting the adhesion of the PR. This means that The spike in the texture height with periodicity across all the etch times in the figure 3.22 is a result of the reduced etch rate at the peaks which are further away from the hole with an increase in P. This results in an increase in the ARp being obtained. This can also explain why the maximum texture height is being obtained for a longer etching time of 20 minutes for the periodicities of 4 and 5 μm, while it is obtained at 18 minutes itself for the lower P.

Table 3.4: Comparison of parameters obtained from different processes

Optimisation step	Texture height (H)	Eq. hole dia (De)	Eq. hole radius (Re)	Re/P	ARp
	nm	μm			
Basic	330	2.8	1.4	0.47	0.11
HB110	370	2.72	1.36	0.45	0.12
HB140	460	2.54	1.27	0.42	0.15
PR thickness	490	2.48	1.24	0.41	0.16
P3 (Optimised)	520	2.42	1.21	0.4	0.17
P4 (Optimised)	750	3.12	1.56	0.39	0.19
P5 (Optimised)	1000	3.78	1.89	0.38	0.2

Thus. the Re/P can be considered as a process parameter which implies the quality of adhesion and texturing process that can be obtained using a particular texturing procedure. The magnitude of the drop in the Re/P that is induced by the tweaking of a parameter implies the impact it has on promoting the quality of the texturing process. Thus, in the above table 3.4, the incorporation of the hard baking step resulted in a major improvement in quality in comparison to the basic recipe. The increase in the PR thickness has also had a positive impact, but the effect is smaller in comparison to the hard baking process. Overall, for a periodicity of 3μm, the optimization of the overall process has improved the process by around 15%. Further increase in periodicity helps in improving the quality of the process by around 2.5% for every additional 1μm increase.

3.6. Analysis of growth of nc-Si on hexagonal textures

The growth of the nanocrystalline silicon (nc-Si) on hexagonal textures was also studied. The figure 3.24 a shows the cross-sectional image of the nc-Si grown along the red and green axes. The columnar growth of grains is visibly seen along both the axes. The height of the nc-Si shown in the images is 2.5 μm, as measured from SEM.

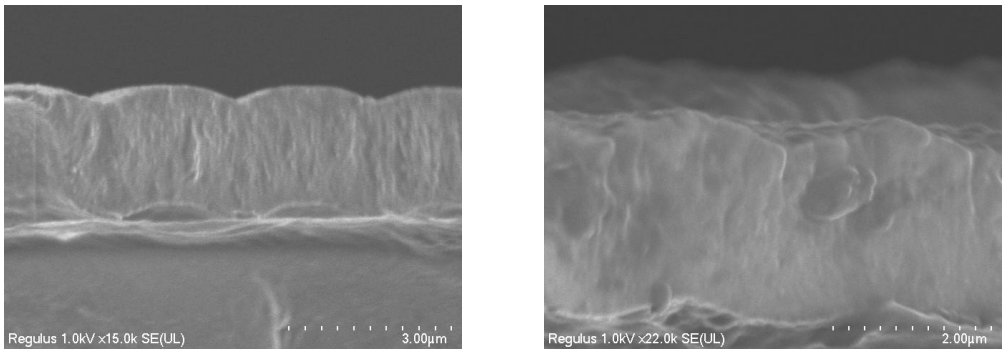

Figure 3.24: Cross sectional SEM image of nc-Si growth on hexagonal textured glass

In the figure 3.25, the top view of the deposition is observed. The growth is conformal in nature and the hexagonal shape is traceable with the grains protruding out of the surface. Also, the grain sizes are approximately 300 - 500 nm,a as visible from the surface. The images did not show any sigifcant cracks with 2.5 μm growth of nc-Si:H.

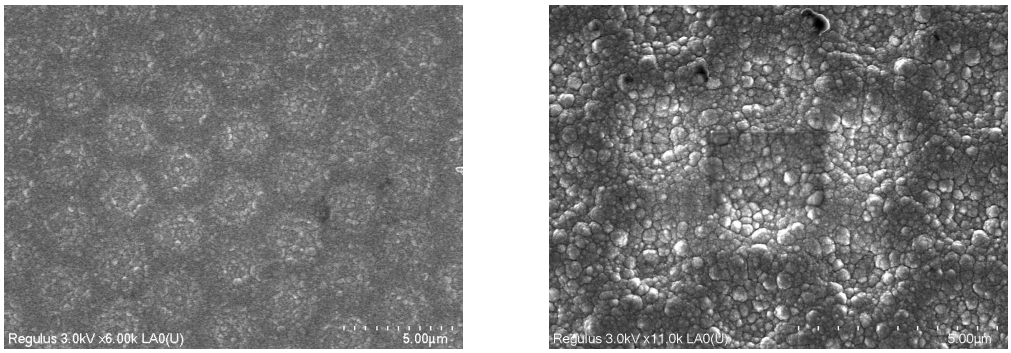

Figure 3.25: Top view of SEM image of nc-Si growth on hexagonal textured glass

4

Optical characterisation of honeycomb texturing

In this chapter, the optical performance of the hexagonal textured glass superstrates obtained in chapter 3 is discussed. The main objective here is to understand the interaction of the hexagonal textured superstrates with light and relate the optical performance of the same to their physical parameters. H.Sai et al. concluded that silicon substrates with hexagonal textures that had an ARp ranging between 0.2 to 0.25 had the most optimum optical performance for application in solar cells[24]. Thierry et al. also studied the optical performance of silicon substrates with periodic texturing by analysing the haze and reflectance AID measurement [25]. They also compared them with the performance of randomly textured silicon substrates and concluded that the optical in-coupling of light was the best for the former. This was mainly due to the additional diffraction effect that was caused by the periodic texturing. Manea et al. observed that the application of hexagonal textures in the front texturing of silicon based solar cells resulted in the front reflectance dropping to below 5% in the visible spectrum of 300 - 700 nm[23].

The optical performance of the samples fabricated has been studied by measuring the total transmittance and diffuse transmittance using the the equipment and methodology specified in section 2.9 in chapter 2. A methodology was also developed to measure the AID of these samples, which will be briefly discussed in section 4.2. Following this, the AID results are analyzed and related to the transmittance measurements in section 4.3. Based on the results obtained in the above-mentioned sections, a relationship has been devised implying the effect of the texture height of the hexagonal textures on the diffuse transmittance (Td) in section 4.4.

4.1. Optical performance of hexagonal textured samples

The optical performance of the hexagonal texturing obtained in the previous chapter were evaluated by measuring the total transmittance (Ttot) and the diffuse transmittance (Td) of the samples developed. This measurement was done over the range of 300 nm to 1100 nm, in steps of 10 nm. The figure 4.1 below shows the total transmittance and diffuse transmittance of all the samples of P 3 μm, 4 μm and 5 μm etched for various durations ranging from 14 min to 24 min in section 3.4.1.

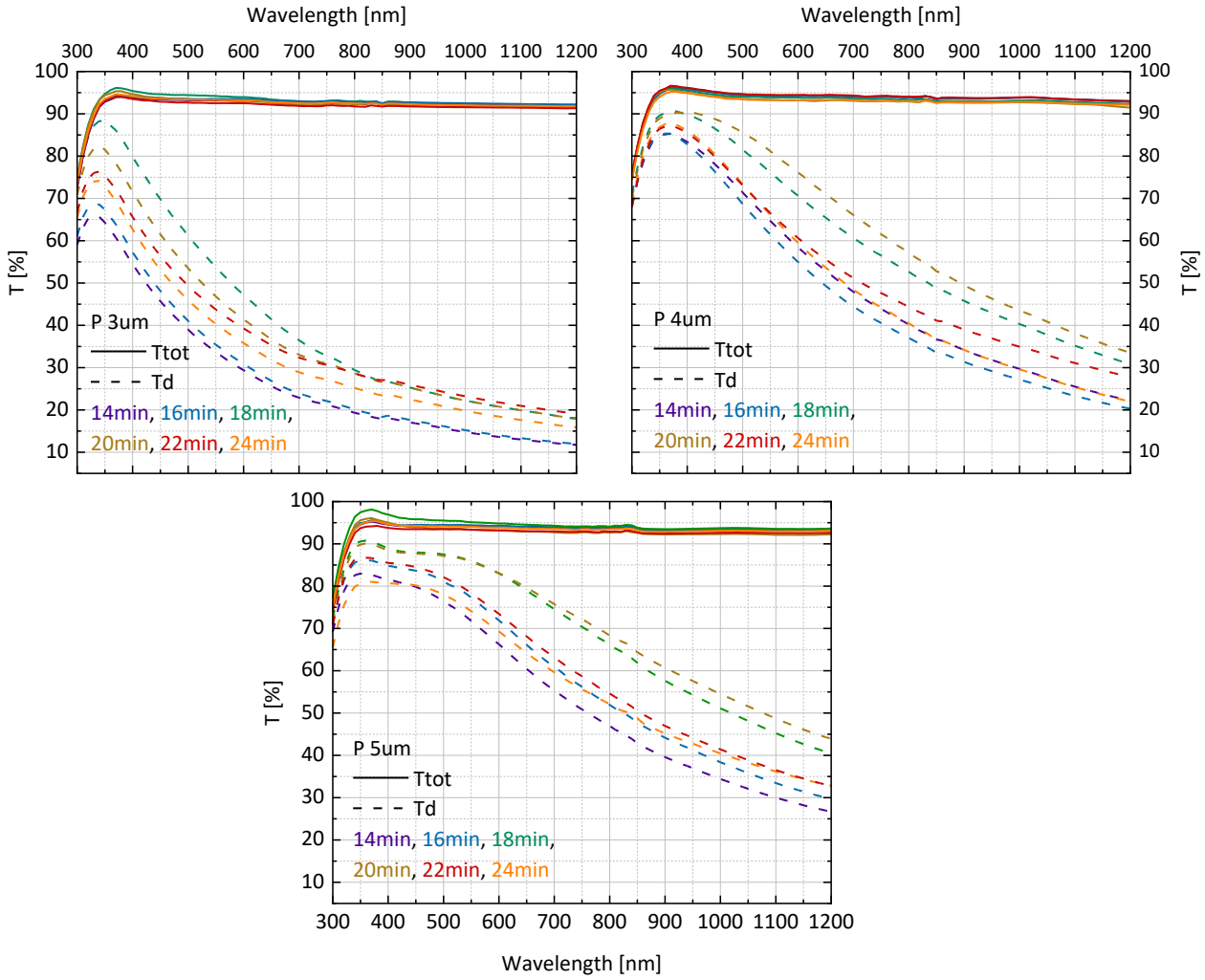

Figure 4.1: Ttot and Td from 300 - 1200 nm for samples etched for varying duration from 14 to 24 minutes; Periodicity of 3 μm (TL) , 4 μm (TR) and 5 μm (Bottom)

From the curves, it is clear the hexagonal textured glass scatters the lower wavelengths better than the higher wavelengths of light, irrespective of the texture height. For the 3μm periodicity samples, it can be seen that the maximum diffuse transmittance is obtained for the sample etched for 18 min. The Td increases with etch time across all wavelengths till the maximum texture height of 520nm. Following this, as the etching further continues the texture height drops and consequently the Td also drops down across the entire spectrum. The 4μm periodicity samples also show a congruent result, where the overall best-performing sample occurs

after etching for 20 minutes, with the deepest texture height of 750 nm. However, it is to be noted that below a wavelength of 400nm, the texture height increase does not result in a major spike in the Td beyond the etch time of 18 minutes, which corresponds to a texture height of 700 nm. This implies that the diffuse scattering for the lower wavelengths increases at a much slower rate with an increase in texture height than the higher wavelengths. This is reiterated in the graph depicting the Td of the samples with 5μm where the texture height increase from 800nm at 16min to 1000 nm at 20 min results in a minor spike at the 400nm wavelength but causes a greater increase at the higher wavelengths near 600nm or above. Thus, it can be seen that the samples with the deepest texture height for the respective periodicity perform the best in terms of optical scattering across all wavelengths.

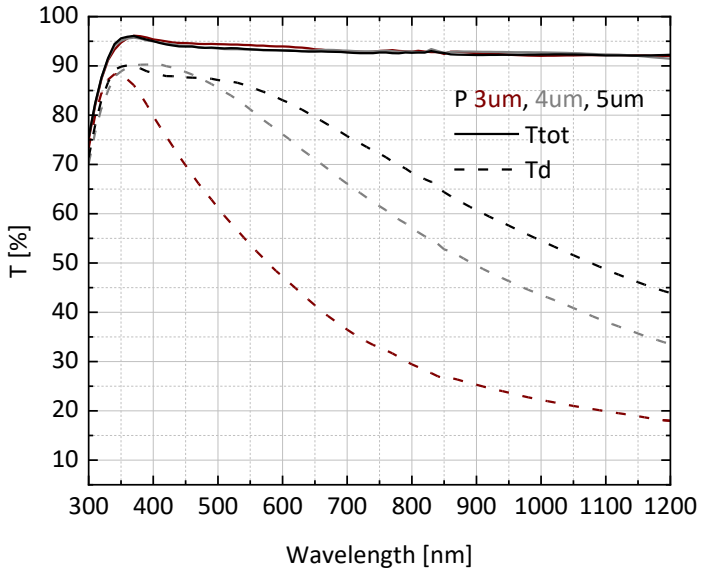

Figure 4.2: Ttot and Td from 300 - 1200 nm for samples with maximum texture height of 520nm, 750nm and 1um and P of 3 μm , 4 μm and 5 μm

The texture height of the best-performing samples from each periodicity is mentioned already in table 3.3 in chapter 3. The figure 4.2 shows the total and diffuse transmittance corresponding to these samples. It can be seen that as the texture H increases the plateau at the peak of the Td extends to higher wavelengths. Thus, the scattering effect peaks for the lower wavelengths at a particular texture height, and the further increase in texture height results in an improvement in the scattering of the higher wavelengths.

4.2. AID measurement methodology for transparent superstrates

To further understand the scattering effect of the texture height on the different wavelengths of light, the Angular Intensity Distribution (AID) is also considered. As mentioned in 2.9, this can be measured in the transmittance (T) or reflectance (R) mode. The first step was to choose the right measurement methodology, which is discussed in the following subsections.

All the AID measurements have been taken in transmittance mode for our analysis. The ARTA offers various modes in which the AID can be measured. The first mode available is the Fixed sample mode, where the sample is fixed at a particular angle, while the detector can be moved through a range of angles from 10 to 350 degrees, in steps of 10 degrees or higher. The range between 350 to 10 degrees is inaccessible for the detector since the source slit is present in this region. The second mode available is the fixed detector mode, where the detector position is fixed and the sample angle can be varied from 0 to 45 degrees, in steps of 10 degrees or higher. The AID for our samples has been measured by using the former mode, where the sample is fixed and the detector is moved across a range of angles. A schematic representation of the setup is shown in figure 4.3 below. The determination of the sampe tilt and detector angle parameters for our analysis is explained in the upcoming sections.

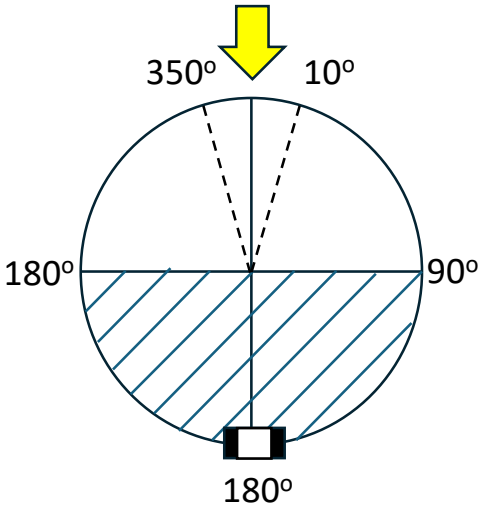

Figure 4.3: Schematic representation of ARTA setup; shaded portion represents detector angle range for ideal case

4.2.1. Determination of detector angle range

As mentioned in section 2.9, the range of the detector angle must be in the second and third quadrants of the detector range. This implies that when the sample is at 0^o tilt, the detector angle range would be between 90^o and 270^o, as shown in image 4.6 a below. However, sometimes, the AID can be measured by tilting the sample angle by a particular tilt angle, as this offers a better interaction of light with the textures in the sample. It is to be noted that the sample is always tilted in the clockwise direction. In such cases, the detector angle range must be modified to cover the second and third quadrants, with respect to the axis passing through the plane of the sample. This can be done by adding a balancing term equal to the tilt angle of the sample to the lower and higher limit of the detector angle range.

So, for instance, if the sample is tilted by an angle of 10^o, as shown in figure 4.6 b below, then a balancing term equal to the tilt angle, which is 10 ^{o} must be added to the limits of the detector angle range. Thus, the actual detector angle range is from 100^o to 280^o.

4.2.2. Determination of best representation of AID

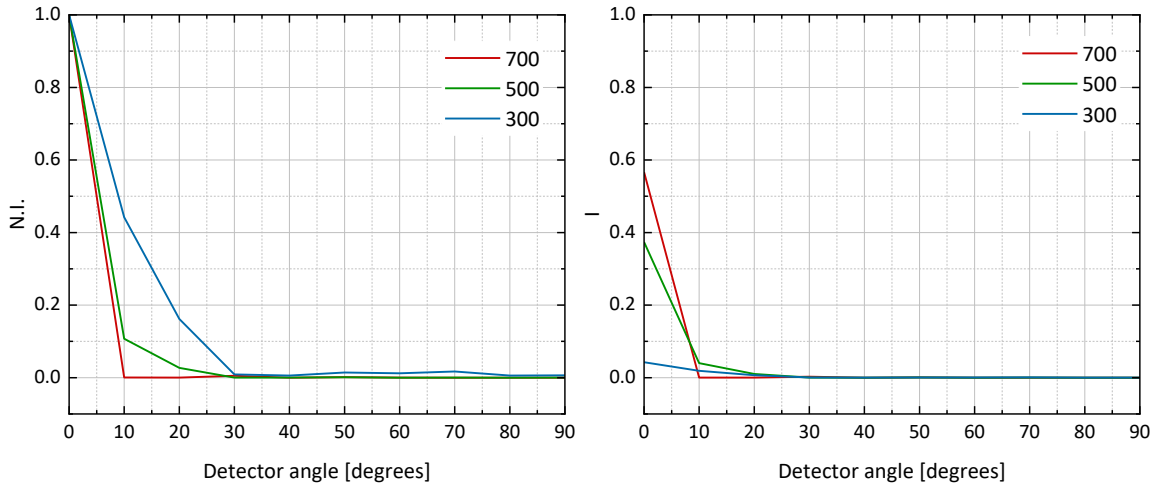

Figure 4.4: Comparison of N.I. and AID for three wavelengths of 300 nm, 500nm and 700nm for sample of H 420 nm and P 3μm at tilt angle of 10^o

The AID measurement was measured for a wavelength range of 300 nm to 900 nm, in steps of 200 nm with the sample angle kept at 10^o for a sample of texture height H 420 nm with a periodicity of 3μm. The reasoning behind the usage of this sample angle will be discussed in section 4.2.3. The AID measurement was also converted to Normalised Intensity (N.I.) by dividing the individual values by the peak value of the AID of each measurement. This was done to identify the representation that would provide an optimum understanding of the variation of the intensity of scattering that the monochromatic light experiences when it interacts with the textured surface. The representation of these values is done from 0 to 90^o, where the angles indicate the position of the detector with respect to the surface vector of the sample (normal from the surface). It is to be noted that only half the hemisphere is depicted since the AID scattering is symmetric about the surface vector.

The figure 4.4 shows the N.I. on the left and the AID on the right, for three wavelengths of 300, 500, and 700 nm for a honeycomb textured sample with a texture height of 420 nm and periodicity of 3 μm, measured at a tilt angle of 10^o. It is to be noted that the peak in both the curves is at 0^o implying that the specular transmission is the highest. This could be caused due to the flat dimple present in the center of the honeycomb textures. From the N.I. it can be clearly seen that the extent of scattering increases for lower wavelengths (at 300nm) and decreases as we move toward the red region. However, the N.I. misses out on the major point that the total specular transmittance portion varies according to wavelength. This is denoted in the AID, which shows that this component increases for higher wavelengths. However, the variation of the scattering across the wavelengths is not visible in the AID.

The figure 4.5 indicates the same data as the AID in the figure 4.4 above, but on a logarithmic scale. This representation provides a culmination of all the information that was obtained from the N.I. and AID graphs shown in figure 4.4. Additionally, the occurrence of peaks can also be seen at certain position angles of the

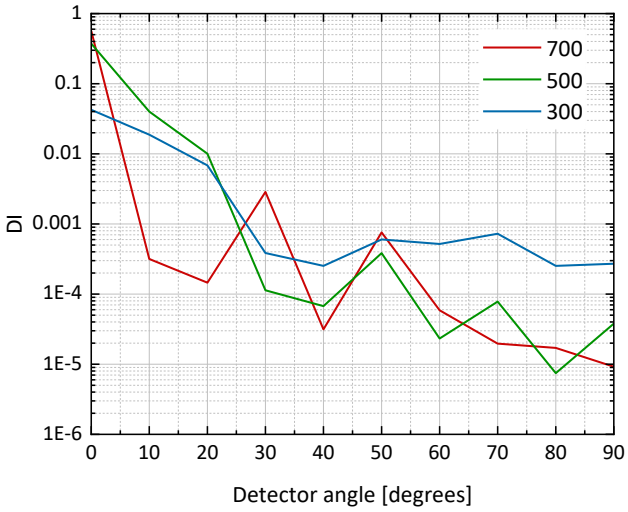

Figure 4.5: AID for three wavelengths of 300 nm, 500nm and 700nm for sample of H 420 nm and P 3μm at tilt angle of 10^o on a logarithmic scale

detector. The magnitude of these peaks increases with wavelength, implying that the intensity of the diffracted light increases with an increase in the wavelength for the same texture height. These aspects will be further looked into in section 4.3.

4.2.3. Determination of sample tilt angle

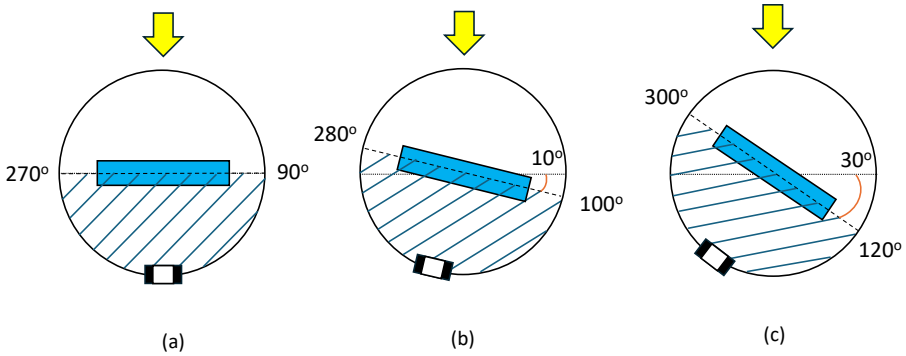

Figure 4.6: Schematic representation of the setup for measuring AID at different sample tilt angles of 0^o, 10^o and 30^o (from left to right)

Since the detector angle range is mainly determined by the tilt angle of the sample, it is essential to choose the optimum value for the same. The previous work done by Crel M and Thierry et al. was analyzed for determining the same [25] [21]. The sample angles of 0^o and 30^o were utilized by Crel M. for studying the scattering effect of hexagonal textured glass. They concluded that the latter sample angle was better for comparison as it provided higher intensities of light across all the wavelengths, resulting in a better perspective of the scattering effect[21]. Thierry et al. used a sample angle of 10^o to analyze the reflectance in silicon-based substrates with hexagonal texturing[25]. To determine the sample tilt angle for our analysis, the AID transmittance was measured for a particular sample with an H of 420 nm using the three different orientations shown in figure 4.6 for the wavelength range from 300 to 900 nm, in steps of 200nm. The AID curves of the same are shown below in figure 4.7 below.

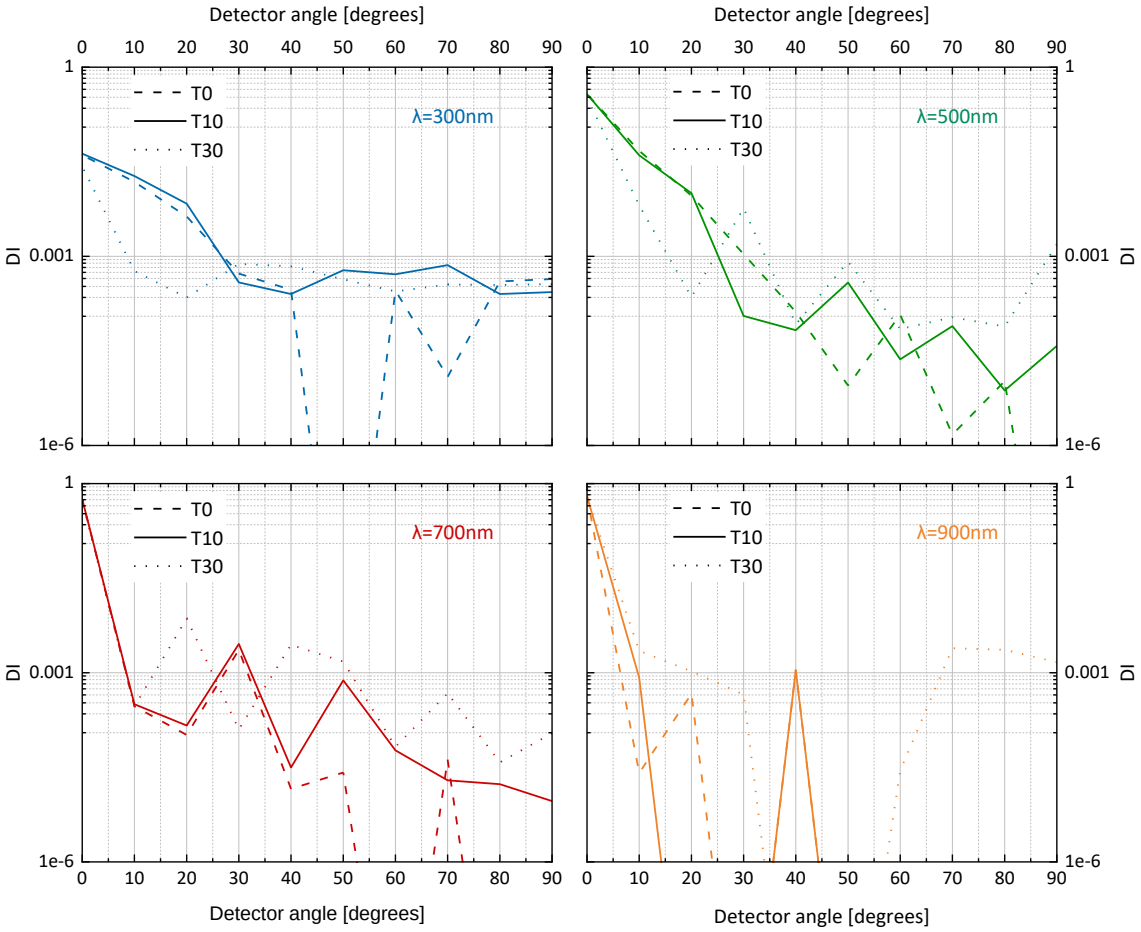

Figure 4.7: AID for wavelengths of 300 nm (TL), 500nm (TR), 700nm (BL) and 900nm (BR)for sample of H of 420 nm and periodicity 3μm at tilt angles of 0^o, 10^o and 30^o on a logarithmic scale

The AID with a tilt angle of 0^o would be the ideal measurement since it is the closest representation of the actual application of the texture where the light beam would be predominantly incident along the normal to

the sample. However, it can be seen that the AID measured with a tilt angle of 10^o provides a similar pattern with the peak intensities being measured more effectively at the higher angles of the detector. This can be noted by the presence of the peaks in the range of 40^o to 80^o for the T10 curves, in comparison to the T0 curves at all wavelengths measured. It is to be noted at higher wavelengths of light, the T30 produces peaks of intensities even higher than that of T10. However, there is a shift in the occurrence of the peaks for the T30 curves in comparison to the ideal T0 case. Thus, the sample angle of 10^o gave an optimum balance, offering prominent peak intensities while also adhering to the curve shape of the T0 case. Hence, this sample angle was chosen for all the AID measurements in the forthcoming sections.

4.3. Influence of texture height on AID

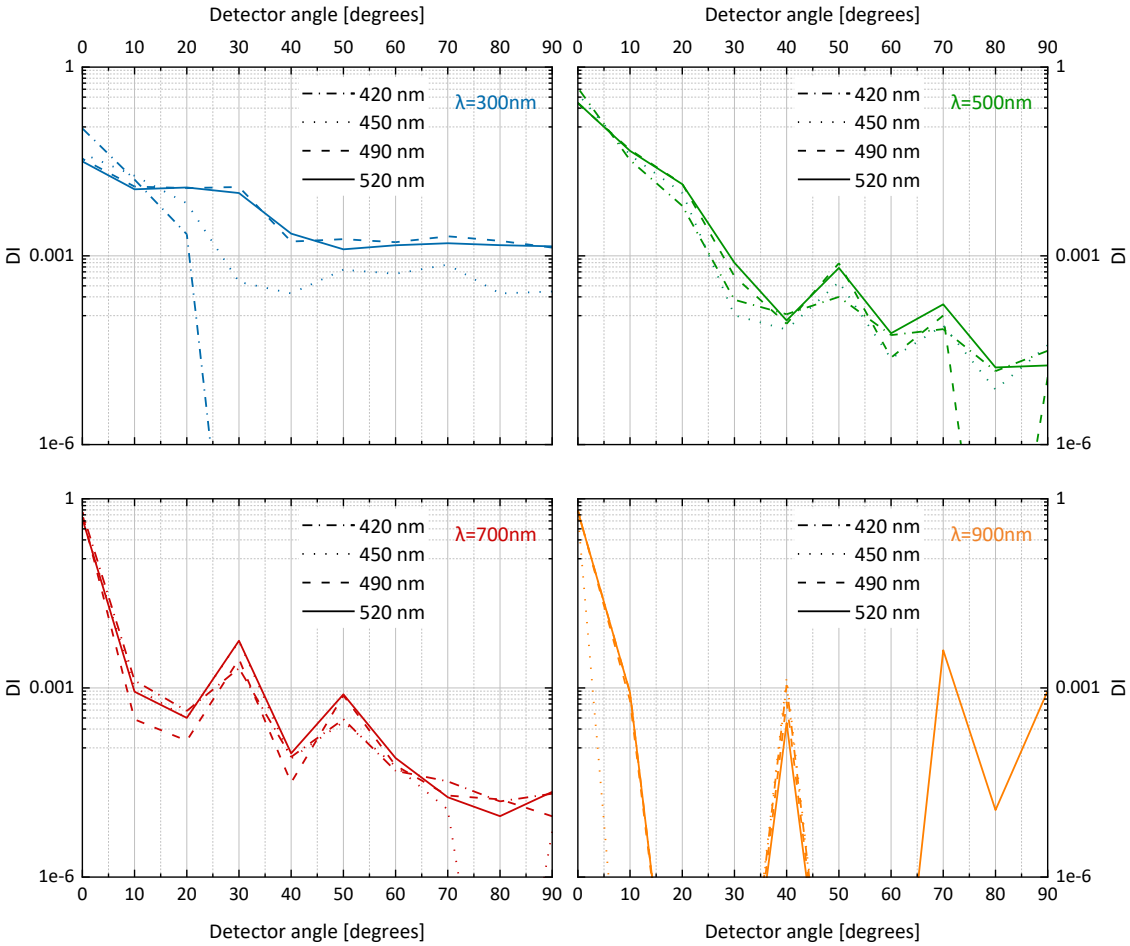

Figure 4.8: AID for wavelengths of 300 nm (TL), 500nm (TR), 700nm (BL), and 900nm (BR) for a sample of H of 420 nm, 450 nm, 490 nm and 520 nm and periodicity 3μm at a tilt angle of 10^o on a logarithmic scale

To study the influence of the texture dimensions on the scattering of different wavelengths, the AID of four samples of H 420 nm, 450 nm, 490 nm and 520 nm with the same P of 3μm was measured in the transmittance mode. These samples were chosen since they had a uniform division of texture height across the same periodicity. For these measurements, the sample angle was taken as 10^o and the appropriate detector angle range was chosen. The setup was similar to the schematic representation in figure 4.6 b. The AID of these samples was measured over a wavelength range of 300 to 900 nm, in steps of 200 nm. The detector angle step size was kept as 10^o. The AID measurement of the same is represented on a logarithmic scale in figure 4.8. The total transmittance and diffuse transmittance of these samples were also measured from the range of 300 nm to 1200 nm, in steps of 10 nm. This is represented below in figure 4.9

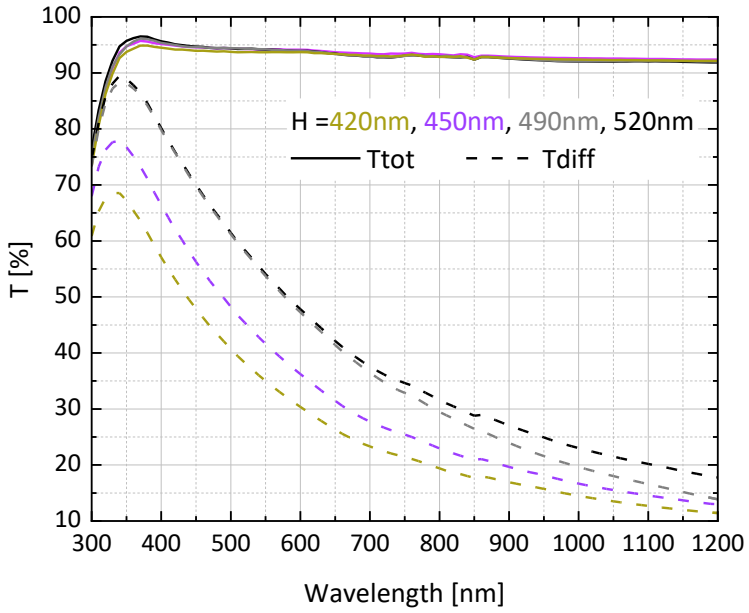

Figure 4.9: Total transmittance (Ttot) and Diffuse transmittance (Td) of four samples of H 420 nm, 450 nm, 490nm and 520nm

For the 300 nm wavelength light, it can be seen that the specular component of the transmission reduces with an increase in the H. However, the scattering effect increases with an upward trend in the H, indicated by the increase in the diffuse intensity at the higher scattering angles above 40^o for the H curves of 490 nm and 520 nm. In the case of the wavelength of 500nm, a slight decrease occurs in the spectral component while for the 700nm light, the spectral component remains unaffected by the H. However, the diffraction peak intensities tend to increase with an increase in the H. It is also to be noted that the first-order and the second-order diffraction peaks are separated by a phase of 20^o for both wavelengths. This implies that the scattering and the diffraction effect of the textures is boosted by an increase in the depth of the textures. In the case of the 500nm light, it can be seen that the zeroth order peak is distributed widely extending till 20^o while the first

and the second order peaks occur around 50^o and 70^o respectively. However, for the higher wavelength of 700nm, the zeroth peak is narrower. Also, for this wavelength, the diffraction peaks occur closer to the zeroth order peak, around 30^o and 50^o. For the 900 nm, a similar pattern can be observed. where the first-order peak intensity remains effectively the same, and a second-order peak occurs for the highest H of 520 nm. It is to be noted that the drop in the intensity at 10^o for the H of 450 nm is considered to be an outlier.

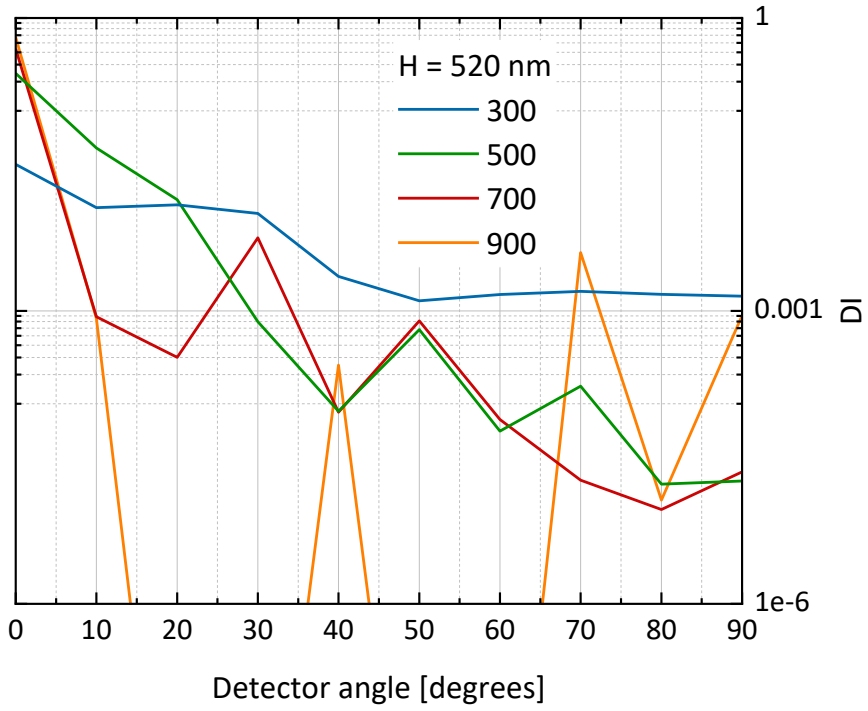

Figure 4.10: AID for wavelengths of 300 nm, 500nm, 700nm and 900nm for sample of H of 520 nm and periodicity 3μm at tilt angles of 10^o on a logarithmic scale

This reiterates our conclusion that for a hexagonal texture of any texture height, as the wavelength of the light increases the scattering effect induced by the texture on it decreases. This can also be seen from the drop in the diffuse transmittance as the wavelength increases for all the four H curves in figure 4.9. However, for the same texture height, as the wavelength of the light interacting with it increases, the diffraction becomes more dominating in spreading the intensity across the span. This can be seen in the figure 4.10 where the scattering of the higher wavelengths is mainly due to diffraction. As the H increases for a texture of the same periodicity, the intensity of the light getting scattered increases across the entire scatter range. This increase in scatter intensity with texture height along with the diffraction results in an increase in the overall scattering for the higher wavelengths. However, for wavelengths above 700 nm, the increase in texture height does not result in a great increase in the scattering, as seen in figure 4.8. It is only the diffraction intensity variation with the texture height increase that causes the small increase in the Td values for these wavelengths shown in figure 4.9.

4.4. Influence of texture height on Td

This increase in scattering stagnates after a particular texture height dependent on the wavelength of light. This relationship can be seen in the figure 4.11 below, which depicts the Td obtained at wavelengths of 300nm, 500nm, 700nm, 900nm and 1100 nm for all the samples obtained from the optimized recipe. It can be seen that there is a linear relationship between the texture height H and the diffuse transmittance Td. As the texture height increases, the Td also increases for all wavelengths. However, the slope of the linear relationship is lower for the wavelength of 300 nm and increases as we move to higher wavelengths till 700nm, following which it decreases to 1100 nm.

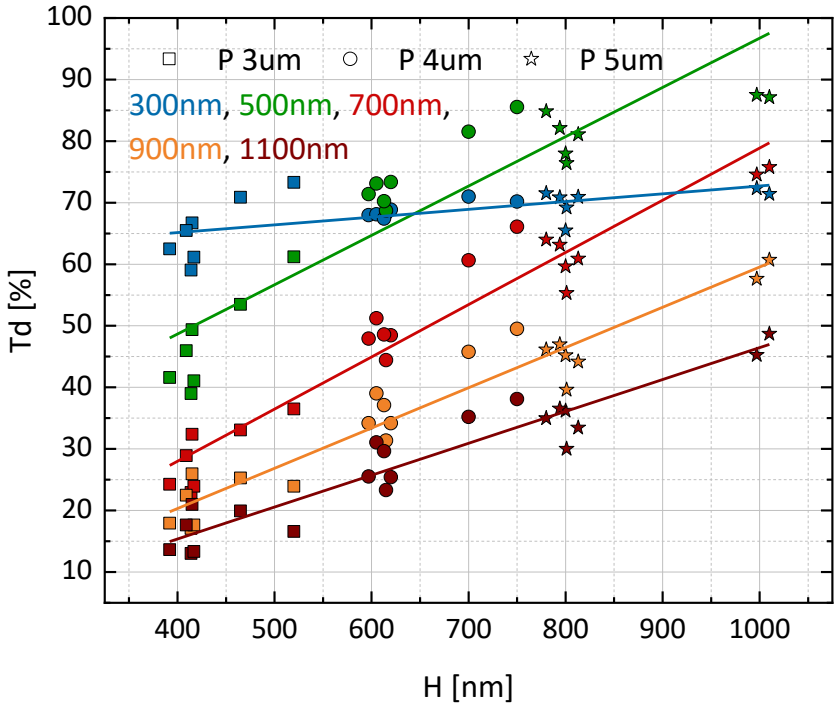

Figure 4.11: Realtionship of Td with H for all P

The increase in the case of the 300 nm is smaller, with the Td stagnating after a texture height of 520 nm.. This is in concurrence with the AID variation that was seen in section 4.3 already. From figure 4.1, when we consider the high energy low wavelength light, for each periodicity, the sample with the best ARp is the optically optimum, in terms of diffuse transmittance. From figures 3.20 and 3.22, it is also deduced that for a particular time series, the samples with the highest ARp also have the maximum height difference between the R and G axes. From figures 4.8, it can be noted that the lower wavelength light gets scattered over a wide angle, which is a characteristic of Rayleigh scattering. As mentioned in section 2.3.2, rayleigh scattering mainly occurs due to the interaction of the low wavelength light with particles of smaller size. From figure 3.6, it can be seen that along the R axis, the peaks of subsequent honeycombs are separated by a small

dip, which has a height equivalent to the height difference between the G and R axes. The height of these shallow features remains the same across all periodicities and ranges from 90 - 125 nm for all ARp values. Thus, these shallow features along the R axis are responsible for the scattering of the low wavelengths and the minor difference between their heights results in the diminished slope value of Td for 300 nm light in figure 4.11.

For the samples with P of 3 μm, the Td is the highest for the low wavelength of 300 m and drops down with increase in wavelength till 1100 nm for all texture heights. However, in the case of the 4μm samples, the Td for 500 nm exceeds that of 300 nm. Similarly, in the case of the 5μm samples, the Td of both 500 nm and 700 nm exceeds the value corresponding to 300 nm. This is because the slope of the low energy high wavelength light increases with texture height as a result of feature size scattering. As seen in figures 4.10 and 4.8, these wavelengths are scattered over a lower span of angles at all texture heights. The increase in the Td can be explained by the combined effect of the increase in scattering and diffraction that occurs with the increase in texture height and breadth of the honeycombs. However, for even higher wavelengths like 900nm and 1100nm, it can be seen that the slope of the increase with H drops. This could be because, at these wavelengths, the diffraction intensity is mainly accentuated by the texture height. However, the dispersion across the entire scatter range is not greatly improved. Thus, for higher wavelengths, the mie scattering takes over and the T is directly impacted by the height of the texture.

4.5. Performance of solar cells with hexagonal textured superstrates

4.5.1. Fabrication of Solar cells

At the later stage of this study, solar cells were made to understand the optical performance and effectiveness of hexagonal textures. Micromorph tandem solar cells were made in PIN superstrate configuration with the size of 5mm x 5mm. The top cell of the solar cell is an amorphous silicon absorber of 300nm, and the bottom cell absorber is nanocrystalline silicon of approximately 2800nm thickness. The deposition was done on a plasma-enhanced chemical vapor deposition (PECVD) tool. The solar cells have a back reflector made of intrinsic Zinc Oxide - 60nm and an Ag/Cr/Al layer. Boron doped p layer, intrinsic amorphous silicon, and Phosphorous doped n layer were deposited with Radio-frequency (13.8MHz) PECVD. The intrinsic nanocrystalline absorber layer was deposited at 40.68MHz. The solar cells are made with front TCO as indium-doped Tin Oxide. ITO is deposited at an elevated temperature of 206^{o}C.

4.5.2. Characterization of solar cells

The Short Circuit Current Density (Jsc) and reflectance measurements are considered as a matrix to quantify the optical response of the substrate. Reflectance measurements were carried out using a LAMBDA 1050+ UV/Vis/NIR Spectrophotometer with a 150mm InGaAs integrating sphere from PerkinElmer. Jsc values were calculated based on their External Quantum Efficiency measurement to prevent overestimation caused by errors in precisely accounting for the active cell area for small-area solar cells.

The External quantum efficiency of three different solar cells made on different periodicity substrates is

shown in Figure4.12. Irrespective of the periodicity, three samples have shown a very high transmissivity throughout the wavelengths. The 1-R curves show very minimal interference fringes. This also suggests that the hexagonal texture scatters light effectively throughout the wavelengths. It is also observed that at near infra-red region the reflectance decreases with an increase in periodicity. Thus the superstrates are optically high-performing. The solar cells made on hexagon textures with periodicity 3um, 4um, and 5um have shown a total spectral utilization of 18.3mA/cm2, 21.7mA/cm2 and 19.9mA/cm2 respectively. 4P is the best optically performing among the three. The solar cells have also shown a very high parasitic absorption, which is assumed to be due to the thick ITO used combined with light coupling by honeycomb textures. This assumption is made from observing a large amount of parasitic absorption in the far infrared wavelengths in EQE. The deposition rate of the TCO, p-doped, and n-doped layers need to be optimized for hexagonal textures (There is a high chance that the deposition rate of hexagon craters is faster compared to other random textures used for PIN depositions). This study was not conducted during this thesis due to the limitation in time.

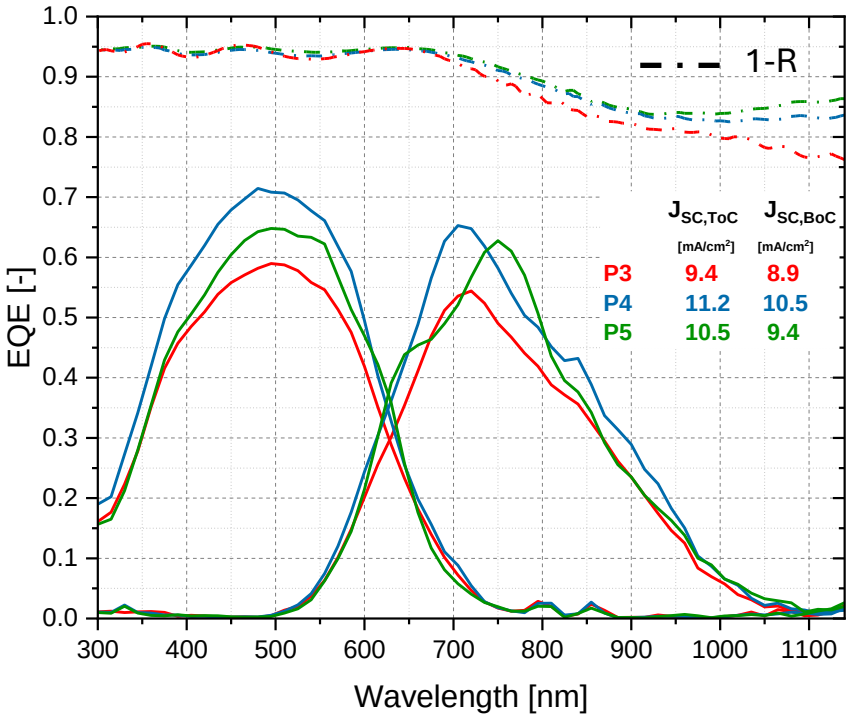

Figure 4.12: EQE and 1-R curves of micromorph solar cells developed on hexagonal textured glass with periodicities of 3μm, 4μm and 5μm

4.6. Additonal application of hexagonal textured glass

The work in this project has been heavily focused on the hexagonal texturing of the glass superstrates for application in thin film silicon solar cells. However, there is countless other applications for the same as well.

An additional application for the deep ARp honeycomb textured glass is as front texturing in c-Si solar cells. Le Chen et al. investigated the transmittance and reflectance properties of periodic textured glass with ARp in the range of 0.2 - 0.5. They concluded that frosted glass with a periodic texturing with ARp of 0.3 offered a reduction in reflectance of almost 40% and increased the transmittance, as well [38]. The resulting samples had an average reflectance of 7.45%. Similarly, the work done by Y. Wang et al. for optimising the periodic texturing in Titanium resulted in reducing the average reflectance of the surface to around 8% [22]. The figure 4.13 shows the front reflectance of the deepest samples from each periodicity of 3μm, 4μm and 5μm. It can be seen that with the drop in the texture size, i.e. the texture height and width (same as periodicity), the front reflectance decreases. Thus, the reflectance mainly occurs as a result of the macroscopic interaction of light with the texture size, as mentioned in 2.4. An average reflectance of 7.93% has been obtained for the 3μm samples, while the higher periodicites offer an average reflectance of 8.14%. Since these values are comparable to the optimum values mentioned presviously, the application of the same in front texturing in PV and other applications can be considered.

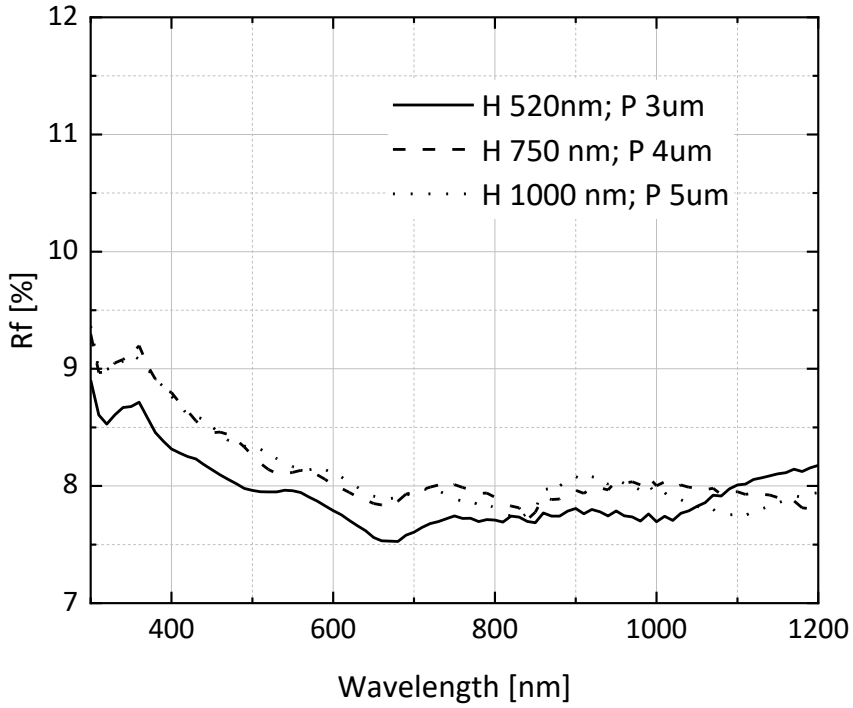

Figure 4.13: Front reflectance of hexagonal textured samples with P of 3μm, 4μm and 5μm having the highest ARp

Another prosperous application for hexagonal textured glass is in the BIPV (Building Integrated Photovoltaics), as mentioned by Bjorn et al [39]. BIPV involves photovoltaic components being used to replace the building blocks in architecture. This promotes the aesthetic nature and also adds to the energy stability of the built environment. The various categories of BIPVs that are employed include photovoltaic foils, photovoltaic tiles, photovoltaic modules, and solar cell glazings. Thin film solar cells, owing to their flexibility can be incor-

porated readily into BIPV. The usage of colorful periodic texturing in such solar cells can help to boost their efficiencies and also beautify the environment.

Also, Roth et al has concluded from their analysis of soiling impact on PV modules, that the PV modules without anti-soiling coatings had a lesser extent of soiling upto 45 days when deep textures were incorporated to the front surface. This could also be an additional scope that can be considered for large scale application, owing to the repeatability of the texturing process [40].

5

Conclusion and Outlook

As a part of this project, a detailed analysis has been done of the various processes involved in the incorporation of hexagonal texturing in glass superstrates. The influence of the various associated parameters like cleaning and preparation of the superstrates, HMDS priming, soft baking, hard baking and PR thickness on the texturing process has been extensively studied and documented. The necessity of appropriate superstrate preparation before photolithography was observed. This was done by cleaning the glass superstrates in 69.5% HNO_3 followed by a running water dip and drying. Different baking steps were also employed at different stages of photolithography for specific applications. The pre-baking of the samples before coating with photoresist was to be done at 110^{o}C for 10 minutes to ensure the removal of adsorbed water. Post development, the samples were to be hard baked at 140 ^{o}C for 30 minutes as this resulted in enhanced PR adhesion via cross-linking. Additionally, it was also noted that during the coating step, it was essential to prime the surface with HMDS at 150^{o}C for 150 seconds to ensure the removal of the polar hydroxyl groups on the surface and to improve the wettability of the surface by the PR. The usage of a thicker PR was also observed to be beneficial as it reduced the diffusion of the etchant ions through the PR. Based on this analysis, an optimized recipe which is a culmination of all the best performing parameters has been developed. Using this, glass superstrates with a deep aspect ratio in the range of 0.17 - 0.2 have been developed, with varying periodicities from 3 to 5 μm.

The growth of nanocrystalline silicon on hexagonal textures of different periodicities was observed and it was concluded that the growth did not result in the formation of cracks up to a thickness of 2,5 μm for all periodicities. Further study can be done to understand the impact of the texture aspect on the growth quality. It could also be interesting to critically observe if there is a thickness limit for the nanocrystalline silicon beyond which crack formation could occur, for hexagonal textures of particular periodicity.

Following this, the influence of the periodicity in the reticle used during photolithography on the texturing

process has also been studied. Based on this, a parameter based on the equivalent hole radius, Re has been developed to indicate the effectiveness of the texturing process, in comparison to the ideal scenario across all periodicities. A relationship has been devised between the expected ARp for a particular hole dia and periodicity, based on the Re/P. Irrespective of periodicity, when a hole dia of 1 μm is used the best Re/P ranges between 0.4 to 0.38 and the corresponding ARp ranges from 0.17 to 0.2. The impact of the variation in the hole diameter in the reticle on the texturing has not been studied and can be looked into further, to achieve hexagonal texturing in superstrates with a higher AR above 0.2. The impact of the same on the Re/P can be looked into and compared to the effect of periodicity.

The optical performance of the superstrates with hexagonal texturing has been studied by using AID and transmittance measurements. A measurement methodology was developed for the effective AID measurement of the hexagonal textured superstrates in transmittance mode. The AID analysis indicated that the scattering of light by the hexagonal texturing is a coupling of the dispersion and diffraction effect induced by the periodicity of the textures. This is also dependent on the wavelength of the light interacting with the texture. Shallow textures present at the R axis peaks scatter the low wavelengths, which stagnate after a texture height of around 520 nm. For wavelengths of 500nm and 700nm, the increase in texture height results in an increase in diffraction coupled with macroscopic focusing of light. This causes the diffuse effect on these wavelengths to increase linearly with a larger slope in comparison to the lower wavelengths. For the higher wavelengths, the increase in texture height results only in an improvement in the diffraction intensities, thereby resulting in a reduced increase in the scattering effect with height. A linear relationship has been discovered between the texture height and the diffuse transmittance across all wavelengths. The slope of this linear relationship is wavelength-dependent due to the variation in the interaction of the texture height with the scattering and diffraction effect of the same.

The optical performance of micromorph solar cells fabricated on the high aspect ratio hexagonal textured superstrates was also studied. For the higher wavelengths, the increase in reflectance was minimal, around 10% for the highest periodicity of 5μm, while it was around 12% and 15% for the 5μm and 3μm respectively. However, the EQE curves of these solar cells implied that the solar cell with 4μm periodicity performed the best. This is mainly an effect of the deposition parameters used in the preparation of the solar cells. Further work is to be done on the optimization of these parameters to reduce parasitic absorption and enhance the quality of these solar cells.

References

[1] IEA (International Energy Agency), “Renewables 2023 - Analysis and forecast to 2028,” Tech. Rep. [Online]. Available: www.iea.org.

[2] H. Victor Du John, D. Jackuline Moni, and D. Gracia, “A detailed review on Si, GaAs, and CIGS/CdTe based solar cells and efficiency comparison,” *Przeglad Elektrotechniczny*, vol. 96, no. 12, pp. 9–18, 2020, ISSN: 24499544. DOI: 10.15199/48.2020.12.02.

[3] A. Smets, K. Jager, O. Isabella, R. van Swaaij, and M. Zeman, *Solar Energy - The physics and engineering of PV conversion technologies and systems*. Delft, Netherlands, 2015.

[4] T. D. Lee and A. U. Ebong, *A review of thin film solar cell technologies and challenges*, 2017. DOI: 10.1016/j.rser.2016.12.028.

[5] Q. Xu, Y. Ji, D. D. Krut, J. H. Ermer, and M. D. Escarra, “Transmissive concentrator multijunction solar cells with over 47% in-band power conversion efficiency,” *Applied Physics Letters*, vol. 109, no. 19, 2016. DOI: 10.1063/1.4967376.

[6] *New world record for the efficiency of crystalline silicon perovskite tandem solar cells*. [Online]. Available: https://www.longi.com/en/news/new-world-record-for-the-efficiency-of-crystalline-silicon-perovskite-tandem-solar-cells/.

[7] R. Acharya, “Satellite Signal Propagation, Impairments and Mitigation.,” *Academic Press*, 2017.

[8] “WO2015093966A1 - Patent - Sacrifical etching using i ZnO and AZO,”

[9] D. Y. Kim, R. Santbergen, K. Jäger, *et al.*, “Effect of substrate morphology slope distributions on light scattering, nc-Si:H film growth, and solar cell performance,” *ACS Applied Materials and Interfaces*, vol. 6, no. 24, pp. 22 061–22 068, Dec. 2014, ISSN: 19448252. DOI: 10.1021/am5054114.

[10] MicroChemicals GmbH, “Chapter 01 MicroChemicals ®-Fundamentals of Microstructuring SUBSTRATE PREPARATION,” Tech. Rep. [Online]. Available: www.microchemicals.com/downloads/application_notes.html.

[11] P. M. Dentinger and J. W. Taylor, “Importance of chemistry at the resist-wafer interface for mechanical and lithographic adhesion,” in *Electron-Beam, X-Ray, EUV, and Ion-Beam Submicrometer Lithographies for Manufacturing VI*, vol. 2723, SPIE, May 1996, pp. 249–260. DOI: 10.1117/12.240476.

[12] M. Chodkowski, K. Terpiłowski, and S. Pasieczna-Patkowska, “Fabrication of transparent polysiloxane coatings on a glass support via the sol-gel dip coating technique and the effect of their hydrophobization with hexamethyldisilazane,” *Physicochemical Problems of Mineral Processing*, vol. 56, pp. 76–88, 2020, ISSN: 16431049. DOI: 10.37190/ppmp/126806.

[13] "0252233 - EP87105987B1 - EPO Patent - Process for improving the adhesion of non-polar photoresists to polar substrates,"

[14] C. Willson and M. Stewart, "Photoresists," in *Encyclopedia of Materials: Science and Technology*, K. J. Buschow, R. W. Cahn, M. C. Flemings, *et al.*, Eds., Oxford: Elsevier, 2001, pp. 6973–6977, ISBN: 978-0-08-043152-9. DOI: https://doi.org/10.1016/B0-08-043152-6/01235-3. [Online]. Available: https://www.sciencedirect.com/science/article/pii/B0080431526012353.

[15] *The difference between positive and negative photoresist*, 2020. [Online]. Available: %https://www.microsi.com/blog/the-difference-between-positive-and-negative-photoresist/#:~:text=Both%20positive%20and%20negative%20photoresists,to%20their%20higher%20resolution%20capabilities..

[16] C. A. Mack, "Photoresist Development, part 1," Tech. Rep., 1987. [Online]. Available: https://www.lithoguru.com/scientist/litho_papers/1987_6_Development%20of%20Positive%20Photoresist.pdf.

[17] *What is afm?* [Online]. Available: https://www.nanoandmore.com/what-is-atomic-force-microscopy?gad_source=1&gclid=CjwKCAjwjqWzBhAqEiwAQmtgT3EpEgKuo-mMTuYjnU2JSwbpOVGUQkZRTsLdLX5yPuZpxVR2l_b57RoCLn8QAvD_BwE.

[18] A. Alessandrini1 and P. Facci, "AFM: a versatile tool in biophysics," vol. 16, 2005. DOI: 10.1088/0957-0233/16/6/R01.

[19] W. Zhou, R. P. Apkarian, Z. Lin Wang, and D. Joy, "Fundamentals of Scanning Electron Microscopy," Tech. Rep.

[20] [Online]. Available: https://www.perkinelmer.com/product/lambda-1050-2d-base-inst-no-sw-l6020055.

[21] M. Criel, "The art of texturing glass for Photovoltaics Processing and optical characterisation," Tech. Rep. [Online]. Available: http://repository.tudelft.nl/..

[22] Y. Wang, C. Ke, T. Wu, X. Zhao, and R. Wang, "Nanosecond laser texturing with hexagonal honeycomb micro-structure on Titanium for improved wettability and optical properties," *Optik*, vol. 192, Sep. 2019, ISSN: 00304026. DOI: 10.1016/j.ijleo.2019.162953.

[23] E. Manea, E. Budianu, M. Purica, *et al.*, "Optimization of front surface texturing processes for high-efficiency silicon solar cells," in *Solar Energy Materials and Solar Cells*, vol. 87, May 2005, pp. 423–431. DOI: 10.1016/j.solmat.2004.06.013.

[24] H. Sai, K. Saito, and M. Kondo, *Enhanced photocurrent and conversion efficiency in thin-film microcrystalline silicon solar cells using periodically textured back reflectors with hexagonal dimple arrays*, Oct. 2012. DOI: 10.1063/1.4761956.

[25] T. De Vrijer, M. Wiering, D. Van Nijen, *et al.*, "The optical performance of random and periodic textured mono crystalline silicon surfaces for photovoltaic applications," *EPJ Photovoltaics*, vol. 13, 2022, ISSN: 21050716. DOI: 10.1051/epjpv/2022021.

[26] D. Eisenhauer, H. Sai, T. Matsui, G. Köppel, B. Rech, and C. Becker, “Honeycomb micro-textures for light trapping in multi-crystalline silicon thin-film solar cells,” *Optics Express*, vol. 26, pp. 498–507, 2018. DOI: https://doi.org/10.1364/OE.26.00A498.

[27] D. Resnik, D. Vrtacnik, U. Aljancic, M. Mozek, and S. Amon, “The role of Triton surfactant in anisotropic etching of {1 1 0} reflective planes on (1 0 0) silicon,” *Journal of Micromechanics and Microengineering*, vol. 15, no. 6, pp. 1174–1183, Jun. 2005, ISSN: 09601317. DOI: 10.1088/0960-1317/15/6/007.

[28] MicroChemicals GmbH, “Chapter 01 MicroChemicals ®-Fundamentals of Microstructuring Chemical and Physical Processes in the Resist Film,” Tech. Rep. [Online]. Available: www.microchemicals.com/downloads/application_notes.html.

[29] Shubhava, A. Jayarama, G. K. Kannarpady, S. Kale, S. Prabhu, and R. Pinto, “Chemical etching of glasses in hydrofluoric Acid: A brief review,” in *Materials Today: Proceedings*, vol. 55, Elsevier Ltd, 2022, pp. 46–51. DOI: 10.1016/j.matpr.2021.12.110.

[30] H. C. J. e. a. Park Hyeongsing, “A Review of Wet Chemical Etching of Glasses in Hydrofluoric Acid based Solution for Thin Film Silicon Solar Cell Application,” *Current photovoltaic research*, vol. 5, pp. 75–82, ISSN: 2288-3274. DOI: https://doi.org/10.21218/CPR.2017.5.3.075.

[31] J. H.K, C. Y.D., W. S.W., and K. T. et al, “Effects of chemical etching with nitric acid on glass surfaces,” *Journal of vacuum science and technology*, vol. 19, pp. 267–274, 2001. DOI: https://doi.org/10.1116/1.1333087.

[32] M. Danish, “Contact Angle Studies of Hydrophobic and Hydrophilic Surfaces,” in *Handbook of Magnetic Hybrid Nanoalloys and their Nanocomposites*, Springer International Publishing, 2022, pp. 1–22. DOI: 10.1007/978-3-030-34007-0{_}24-1.

[33] ISO, *ISO 19403 Part 2: Determination of the surface free energy of solid surfaces by measuring the contact angle*. ISO/TC35/SC9, 2017.

[34] Christian, “Baking Steps in Photoresists Processing,” Tech. Rep., 2013. [Online]. Available: www.microchemicals.com/downloads/application_notes.html.

[35] M. P. M. GmbH, “TDS_AZ_eci_3012_photoresist - Technical Data Sheet,”

[36] Christian, “Hardbake of Photoresist Structures,” Tech. Rep., 2013. [Online]. Available: www.microchemicals.com/downloads/application_notes.html.

[37] Christian, “Reflow of Photoresist Revised: 2013-11-07 Source,” Tech. Rep. [Online]. Available: www.microchemicals.com/downloads/application_notes.html.

[38] L. Chen, Q. Wang, W. Chen, K. Huong, and X. Shen, “Investigation of a novel frosted glass with regular pit array texture,” *Journal of materials processing technology*, vol. 238, 2016.

[39] B. Jelle, C. Breivik, and R. H.D, “Building integrated photovoltaic products: A state-of-the-art review and future research opportunities,” *Solar Energy Materials and Solar cells*, vol. 100‘, 2012.

[40] R. Roth, C. Ballif, and V. Chapuis, “Effect of soiling on performances of crystalline silicon pv modules developed in an arid climate in relation to front glass texture and treatment,”

A

Source code - Slope distribution

```
1
2  %import heiught matrix
3  clc
4  clear
5  afm_data=xlsread('18min_xyz_0.xlsx');
6
7  %to find slope matrix
8  %enter x and y value
9  %512 x values for each y
10 x=afm_data(2,1)-afm_data(1,1);
11 %y=afm_data(513,2)-afm_data(512,2); to find y step
12 %X=afm_data(:,1); %to find x points
13 %Y=afm_data(:,2); %to find y points
14
15 Z=afm_data(:,3); %to find height array to compare with height map
16
17 height_map=zeros(512,512);
18 height_map(1,1)=afm_data(1,3);
19 a=afm_data(1,2);
20 i=1;
21 j=1;
22 k=1;
23 while i<262144
24 if afm_data(i+1,2) == afm_data(i,2)
25     height_map(j,k) = afm_data(i,3);
26     i=i+1;
27     j=j+1;
```

```
else
    height_map(j,k) = afm_data(i,3);
    k=k+1;
    j=1;
    i=i+1;
end
end
p=size(afm_data);
height_map(512,512) = afm_data(p(1,1),p(1,2));
%row corresponds to same x and column corresponds to same y
[S1,S2]=slope(height_map,x);

%c1 = height_map(1:j-1,1:k-1); to understand the function


%to find slope dist of S1

min_slope=min(S1);
imin=min(min_slope); %minimum value 9f slope
max_slope=max(S1);
imax=max(max_slope); %max value of slope

occurence_S1=zeros(ceil(imax),1);
i0 = 1;
j0=1;
o=1;

while o <=ceil(imax)
   j0=1;
    while j0< 512
    i0=1;
        while i0 < 512

            if o-1<S1(i0,j0) & S1(i0,j0)<o

                occurence_S1(o,1)= occurence_S1(o,1) + 1;

            end

            i0=i0+1;

        end

        j0=j0+1;

    end

```

```
   o=o+1;

end

%to find slope dist of S2

min_slope1=min(S2);
imin1=min(min_slope1); %minimum value 9f slope
max_slope1=max(S2);
imax1=max(max_slope1); %max value of slope

occurence_S2=zeros(ceil(imax1),1);
i1 = 1;
j1=1;
o1=1;

while o1 <=ceil(imax1)
   j1=1;
    while j1< 512
    i1=1;
        while i1 < 512

            if o1-1<S1(i1,j1) & S1(i1,j1)<o1

                occurence_S2(o1,1)= occurence_S2(o1,1) + 1;

            end

            i1=i1+1;

        end

        j1=j1+1;

    end

   o1=o1+1;

end

%to obtain plots

prob_S1=occurence_S1/sum(occurence_S1);
prob_S2=occurence_S2/sum(occurence_S2);
xlim_S1=ceil(imax);
plot(1:xlim_S1,prob_S1)
yticks(0:0.025:0.15)
```

```
ylabel("S1 distribution")
grid on
hold off
xlim_S2=ceil(imax1);
plot(1:xlim_S2,prob_S2)
ylabel("S2 distribution")
grid on


%Sample loop
%{
Simple loop of splitting height map

A=[1 10;1 8;1 7;2 9;2 15;2 12];
B=zeros(3,2);
i=1;
j=1;
k=1;
while i<6
if A(i+1,1)==A(i,1)
    B(j,k) = A(i,2);
    j=j+1;
    i=i+1;
else
    B(j,k) = A(i,2);
    k=k+1;
    j=1;
    i=i+1;
end
end

%}


%{
simple loop of finding slope dist
A = [1.1 2.1
    3.2 2.2
    4.2 3.3];
B=zeros(5,1);
i0=1;
j0=1;
o=1;
while o<6
    j0=1;
while j0<3
    i0=1;
```

```
    while i0<4

        if o-1<A(i0,j0) & A(i0,j0)<o

            B(o,1)=B(o,1)+1;
        end
        i0=i0+1
    end
    j0=j0+1;
end
o=o+1;
i0=1;
j0=1;
end
%}

function [s1,s2] = slope(AFM,xy)
%SLOPE Calculates and visualizes slope distribution of height map (AFM scan)

%INPUT
% AFM       height map
% xy        spacing of points in x and y direction

[n,m] = size(AFM);

%height map consists of square array of points, so can be
%divided into small square units, each with four corners
    % corner 1 height
c2 = AFM(1:n-1,2:m  );  % corner 2 height
c3 = AFM(2:n  ,1:m-1);  % corner 3 height
c4 = AFM(2:n  ,2:m  );  % corner 4 height

%each square is divided into upper and lower triangle
%slope of surface normal is calculated using cross-product
s1 = atand(sqrt((c1-c2).^2 +(c1-c3).^2)/xy);  %upper triangle slope (degrees)
s2 = atand(sqrt((c4-c2).^2 +(c4-c3).^2)/xy);  %lower triangle slope (degrees)

end
```

B

TDS - Corning glass XG

CORNING

EAGLE XG®

Glass Substrates

Material Information

CORNING

Glass Type – Alkaline earth boro-aluminosilicate
Forms Available – Fusion-drawn sheet
Principal Uses – Substrates for active-matrix flat panel displays

Properties

Where applicable, units are stated in Metric and English

Mechanical

	Metric	English
Density (20°C, 68°F)	2.38 g/cc	148.5 lb/ft^3
Young's Modulus	73.6 GPa	10.7 x 10^6 psi
Shear Modulus	30.1 GPa	4.4 x 10^6 psi
Poisson's Ratio	0.23	
Vickers Hardness (200 gm load, 25 sec dwell)	640	

Thermal Expansion

0 - 300°C	31.7 x 10^{-7}/°C (0 - 300°C)	17.7 x 10^{-7}/°F (32 - 572°F)
Room Temperature	35.5 x 10^{-7}/°C	19.7 x 10^{-7}/°F
To Setting Point	(25 – 675°C)	(77 – 1247°F)

Thermal Conductivity

Thermal conductivity is a calculated value, and is equal to the product of the thermal diffusivity multiplied by specific heat multiplied by the density of the glass.

Temp (°C)	Specific Heat (J/gm- °K)	Thermal Diffusivity (cm^2/sec)	Thermal Conductivity (W/cm-°K)
23	0.768	0.00601	0.0109
100	0.896	0.00572	0.0122
200	0.998	0.00546	0.0129
300	1.067	0.00530	0.0134
400	1.110	0.00522	0.0137
500	1.154	0.00518	0.0142

Viscosity

Working Point (10^4 poises)	1293
Softening Point (10$^{7.6}$ poises)	971
Annealing Point (10^{13} poises)	722
Strain Point (10$^{14.5}$ poises)	669

Electrical

Log_{10} Volume Resistivity (ohm-cm)

12.9 (250°C, 482°F)
8.8 (500°C, 932°F)

Dielectric Constant

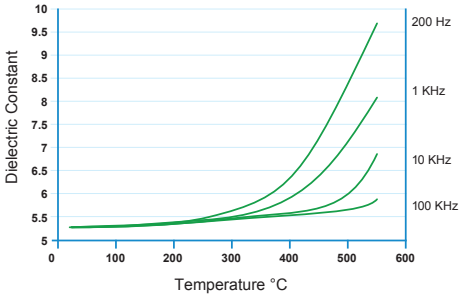

Dielectric Constant: 5.27
(20°C/68°F – 1 kHz)

Dissipation Factor (Loss Tangent)

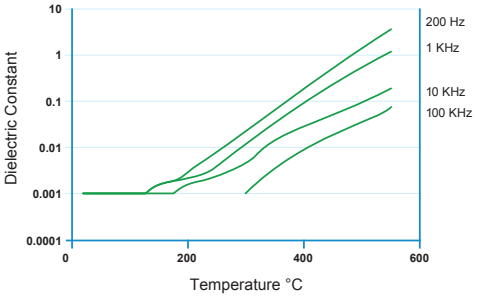

Loss Tangent: 0.30%
(20°C/68°F – 1 kHz)

Chemical

Weathering: 1
Weathering is defined as corrosion by atmospheric-borne gases and vapor such as water and carbon dioxide. Glasses rated 1 will almost never show weathering effects; those rated 2 will occasionally be troublesome, particularly if weathering products cannot be removed; those rated 3 require more careful consideration.

Durability:
Durability is measured via weight loss per surface area after immersion. Values are highly dependent upon actual testing conditions. Unless otherwise noted, concentrations refer to weight percent.

Reagent	Time	Temp	Weight Loss (mg/cm²)
HCl – 5%	24 hrs	95°C	0.79
HNO_3 – 1M	24 hrs	95°C	0.49
HF – 10%	20 min	20°C	5.18
NH_4F: HF – 10%	20 min	20°C	0.84
1HF: 10HNO_3	3 min	20°C	1.48
1HF: 100HNO_3	3 min	20°C	0.16
DI H2O	24 hrs	95°C	0.00
Na_2CO_3 – 0.02N	6 hrs	95°C	0.16
NaOH – 5%	6 hrs	95°C	1.83

Total alkali content is approximately: 0.1 wt%
(Typical < 0.05 wt%)

Optical Wavelength	Refractive Index
435.8 nm	1.5198
467.8 nm	1.5169
480 nm	1.5160
508.6 nm	1.5141
546.1 nm	1.5119
589.3 nm	1.5099
643.8 nm	1.5078

Birefringence Constant

331 (nm/cm)/(kg/mm²)

C

TDS - AZ ECI 3012 PR

Technical Data Sheet

Technisches Datenblatt

AZ ECI 3012 Photoresist

Universal i-Line/Crossover
Photoresist

GENERAL INFORMATION

AZ ECI 3012 photoresist is a fast positive resist with high resolution capabilities (0.4 µm CDs in production in i-line) enabling wide process latitudes. It is suited for i-line as well as broadband exposure covering g-, h- and i-line illumination wavelengths. It is designed to have superior implant and dry etch resistance. Further characterization highlights show strong wet etch adhesion and good thermal stability. This resist is specifically tailored for universal application and excellent cost of ownership.

RECOMMENDED PROCESS

Softbake:	90°C, 60 sec (contact) - 90 sec (proximity)
Exposure:	i- & g-line stepper or broadband exposure
Post Exposure Bake (PEB):	110°C, 60 sec (contact) - 90 sec (proximity)
Development:	60 sec, puddle, AZ® 300 MIF Developer (non surfactated) or AZ® 726 MIF Developer (surfactated)

SUITABLE ANCILLARIES

AZ Aquatar® top anti-reflective coating
AZ BARLi® II bottom anti-reflective coating
AZ EBR 70/30 edge bead remover
AZ 100 Remover or AZ KWIKSTRIP

Merck Performance Materials GmbH
Rheingaustrasse 190 - 196
D-65203 Wiesbaden
Germany
Tel. +49 (611) 962-4031
Email: jasmin.schmicking@merckgroup.com

Technical Data Sheet

Technisches Datenblatt

CAUCHY COEFFICIENTS	A	B	C
Unbleached	1.6018	0.0098963 µm²	0.00068636 µm⁴
	1.6018	9.8963 x 10^5 Å²	6.8636 x 10^{12} Å⁴
Bleached	1.5952	0.0084508 µm²	0.0006556 µm⁴
	1.5952	8.4508 x 10^5 Å²	6.556 x 10^{12} Å⁴

REFRACTIVE INDEX		365 nm	405 nm	435 nm	633 nm
Unbleached	n	1.7014	1.6803	1.6826	1.6308
	K	0.0202	0.0244	0.0166	0
Bleached	n	1.6913	1.6670	1.6530	1.6204
	K	0.0017	0.0010	0	0.0001

DILL PARAMETERS	A	B	C
i-line	0.64 µm^{-1}	0.075 µm^{-1}	0.0159 cm²/mJ
h-line	0.76 µm^{-1}	0.035 µm^{-1}	0.0244 cm²/mJ
g-line	0.45 µm^{-1}	0.036 µm^{-1}	0.0152 cm²/mJ

SPIN CURVE
Softbake: 90°C, 90 sec, proximity
Wafer size: 6” (150 mm)
dynamic dispense

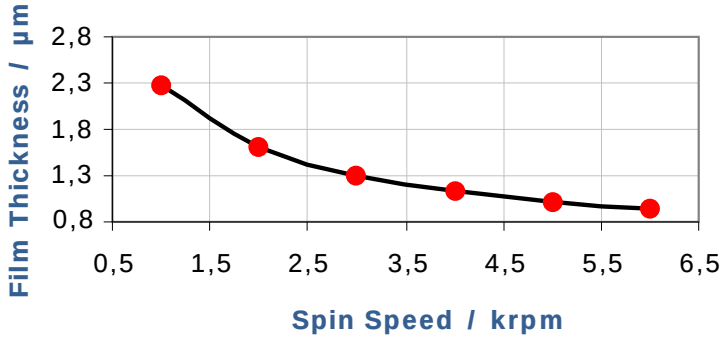

FILM THICKNESS	2000 rpm	3000 rpm	4000 rpm	5000 rpm
	1.61 µm	1.31 µm	1.13 µm	1.02 µm
STD DEV	1.2 nm	0.8 nm	0.5 nm	1.1 nm

Merck Performance Materials GmbH
Rheingaustrasse 190 - 196
D-65203 Wiesbaden
Germany
Tel. +49 (611) 962-4031
Email: jasmin.schmicking@merckgroup.com